Hierarchical Bayesian Modeling of the Relationship between Task Related Hemodynamic Responses and Neuronal Excitability: a Simultaneous fNIRS/TMS Study

Zhengchen Cai[1,2], Giovanni Pellegrino[3,4], Jean-Marc Lina[5,6], Habib Benali[2], Christophe Grova[1,2,4,6]

[1] Department of Physics, Concordia University, Montréal, Québec, Canada
PERFORM Centre, Concordia University, Montréal, Québec, Canada
[2] PERFORM Centre, Concordia University, Montréal, Québec, Canada
[3] Neurology and Neurosurgery Department, Montreal Neurological Institute, McGill University, Montréal, Québec, Canada
[4] Multimodal Functional Imaging Lab, Biomedical Engineering Department, McGill University, Montréal, Québec, Canada
[5] Département de Génie Electrique, École de Technologie Supérieure, Montréal, Québec, Canada
[6] Centre De Recherches En Mathématiques, Montréal, Québec, Canada

Correspondence:
Zhengchen Cai,
Multimodal Functional Imaging Lab,
Department of Physics and PERFORM Centre, Concordia University.
Loyola Campus, Office SP 365.23
7141 Sherbrooke Street West, Montreal, QC, H4B 1R6, Canada
Phone: (514) 848-2424 ext.3393
Corresponding author emails: zhengchen.cai@mail.concordia.ca; zhengchen.cai@gmail.com

Abstract:

Background: Investigating the relationship between task-related cortical hemodynamic activity and brain excitability is challenging because it requires simultaneous measurement of brain hemodynamic activity while applying non-invasive brain stimulation. There is also considerable inter-/intra-subject variability which both brain excitability and task-related hemodynamic responses are associated with. Here we proposed hierarchical Bayesian modeling to taking into account variability in the data at the individual and group levels, aiming to provide accurate and reliable statistical inferences on this research question.

Methods: We performed a study on 16 healthy subjects with simultaneous Paired Associative Stimulation (Inhibitory PAS10, Excitatory PAS25, Sham) and functional Near-Infrared Spectroscopy (fNIRS) targeting the primary motor cortex (M1). PAS was applied to modulate the cortical function and induce plasticity. Before and after each intervention cortical excitability was measured by motor evoked potentials (MEPs), and the motor task-related hemodynamic response was measured using fNIRS. We constructed three models to encode 1) PAS effects on the M1 excitability; 2) PAS effects on the whole-time course of fNIRS hemodynamic responses to finger tapping tasks, and 3) the correlation between PAS effects on M1 excitability and PAS effects on task-related hemodynamic responses.

Results: Significant increase of the cortical excitability was found after PAS25, whereas a small reduction of the cortical excitability was shown after PAS10 and no changes after sham. We found PAS effects on finger tapping evoked HbO/HbR within M1, around the peak of the hemodynamic time courses. Both HbO and HbR absolute amplitudes increased after PAS25 and decreased after PAS10. Cortical excitability changes and task-related HbO/HbR changes showed a high probability of being positively correlated, 0.77 and 0.79, respectively. The corresponding Pearson's correlations were 0.58 ($p<.0001$, HbO with MEP) and 0.56 ($p<.001$, HbR with MEP), respectively.

Conclusion: Benefiting from this original Bayesian data analysis, our results showed that PAS modulates task-related cortical hemodynamic responses in addition to M1 excitability. The fact that PAS effects on hemodynamic response were exhibited mainly around the peak of the hemodynamic time course may indicate that the intervention only increases metabolic demanding rather than modulating hemodynamic response function per se. Moreover, the positive correlation between PAS modulations of excitability and hemodynamic brings insights to understand the fundamental properties of cortical function and cortical excitability.

Keywords: Paired Associative Stimulation (PAS), Excitability, Maximum Entropy on the Mean (MEM), Finger Tapping, Near-Infrared Spectroscopy (NIRS), Transcranial Magnetic Stimulation (TMS), Bayesian Data Analysis.

Highlights:

- Hierarchical Bayesian Modeling of PAS effects on M1 excitability and hemodynamic
- Demonstrated PAS effects on the whole time-course of task-related hemodynamic
- Increased/reduced task-related hemodynamic corresponds to higher/lower M1 excitability
- High probability of positive relationships between excitability and HbO/HbR changes

1 Introduction

The association between hemodynamic response to a task and excitability of the corresponding cortical region helps to understand the relationship between cortical metabolic demand and cortical readiness. This knowledge might be useful to expand the field of application of non-invasive brain stimulation for treating brain disorders in which modulation of hemodynamic activity is desired. Currently, there are several non-invasive brain stimulation techniques capable of interacting with cortical function and are potentially useful to treat neurological conditions. One of the eldest and better-known techniques is repetitive Transcranial Magnetic Stimulation (rTMS): TMS pulses repeated in a train following a certain frequency induce Long-Term Potentiation (LTP)-like and Long-Term Depression (LTD)-like plasticity which are typically measured as changes of cortical excitability (Ridding and Rothwell, 2007; Di Pino et al., 2014). Another way to induce plasticity relies on the concept of Spike Timing Dependent Plasticity (STDP, Levy and Steward, 1983; Rossini et al., 2015) and is entitled Paired Associative Stimulation (PAS) (Mariorenzi et al., 1991; Stefan, 2000). PAS consists of pairs of cortical TMS and peripheral electrical Median Nerve Stimulation (MNS) delivered with proper timing: around 25ms or 10ms Interstimulus Intervals (ISI) to excite (PAS25) or to inhibit (PAS10) primary motor cortical areas, respectively. The peak-to-peak amplitude of Motor Evoked Potentials (MEPs) measured by electromyography (EMG) on the hand muscle is often used to assess the cortical excitability while delivering single pulse TMS (spTMS) on top of the primary motor cortex (Suppa et al., 2017).

In animal studies, by applying invasive optical imaging, Allen et al. (2007) demonstrated that low-frequency repetitive rTMS, known for reducing cortical excitability, on cat's visual cortex induces an immediate increase of tissue oxygenation followed by a prolonged reduction of oxygenation lasting approximately 2 minutes. More recently, a study on healthy rats combining functional Magnetic Resonance Imaging (fMRI) and proton Magnetic Resonance Spectroscopy (MRS) showed increases in resting-state connectivity (e.g., Interoceptive/default model network, cortico-striatal-thalamic network and Basal ganglial network), GABA, glutamine and glutamate levels following high-frequency rTMS (known for increasing cortical excitability) and reduced connectivity and glutamine levels after low-frequency rTMS stimulations (Seewoo et al., 2019).

In human studies, similar investigations become more challenging which require the combination of non-invasive neuroimaging and non-invasive brain stimulation approaches.

For instance, fMRI (Bandettini et al., 1992; Kwong et al., 1992; Glover, 2011) is a widely used modality to measure the hemodynamic activity and can measure the hemodynamic fluctuations related to TMS interventions (Navarro De Lara et al., 2015; Tik et al., 2017). However, simultaneous fMRI/TMS acquisitions require specific MRI coil and fMRI sequences (Navarro De Lara et al., 2015; Wang et al., 2017). This is the reason why most studies consisted in fMRI sessions before and after TMS interventions, following a so-called offline approach (Siebner et al., 2009).

Alternatively, functional Near-InfraRed Spectroscopy (fNIRS) non-invasively measures fluctuations of both oxygenated- and deoxygenated-hemoglobin (i.e., HbO and HbR) concentration changes in the human brain with a high temporal resolution (Jöbsis, 1977; Scholkmann et al., 2014). fNIRS relies on optical absorption which is insensitive to electromagnetic fields, as opposed to fMRI. Therefore, fNIRS appears as an interesting alternative offering better compatibility for simultaneous acquisition during TMS (Curtin et al., 2019). In Cai et al., 2021b, we conducted a simultaneous PAS-fNIRS study to investigate the relationship between motor task-evoked cortical hemodynamic response and M1 excitability. We opted for PAS rather than rTMS for multiple reasons. A previous simultaneous TMS/fNIRS study reported that physiological fluctuations of respiration and heart rate are largely influenced by trains of TMS pulses (Näsi et al., 2011). In other words, TMS trains may influence both systemic hemodynamic (scalp signal) and cortical hemodynamic responses. Second, the frequency of stimulation pairs in PAS is 0.1Hz or less (Suppa et al., 2017), therefore PAS intervention is likely introducing significantly less or even no systemic physiological fluctuations when compared to rTMS. Third, when several stimulations with multiple effects are applied (excitatory, inhibitory, sham), PAS offers stimulations that are similar with respect to duration and frequency across conditions, allowing a more balanced and cleaned experiment design.

Beyond the technical difficulties of addressing the relationship between excitability and hemodynamic activity, one main challenge lies in the high intra- and inter-subject variability of both the effects of brain stimulation and the hemodynamic activity associated with a task. The ability of PAS in eliciting significant changes in cortical excitability has been replicated by several studies (Stefan, 2000; Wolters et al., 2005; Tsang et al., 2015; Lee et al., 2017; Suppa et al., 2017), but some studies have observed that only 39% of subjects showed expected MEP amplitude increase after conducting PAS25 (López-Alonso et al., 2014) and similar PAS efficiency (lower than 50%) has been suggested in a review study (Suppa et al.,

2017). Similarly, inter-subject variability of the task-evoked hemodynamic response has also been reported, whether measured using fMRI (Witt et al., 2008) or fNIRS (Novi et al., 2020). These variability issues may explain the negative findings on the correlation between cortical excitability and hemodynamic activities. For instance, Kriváneková et al., (2013) investigated the relationship between the primary motor cortex (M1) excitability and Blood-Oxygen-Level-Dependent (BOLD) signal using PAS stimulation and "offline" fMRI acquisitions. They reported no significant correlation between PAS effects on task-related BOLD response and its effects on M1 excitability. In our previous study (Cai et al., 2021b), using fNIRS and PAS we first found a significant positive correlation between fluctuations of cortical excitability (represented by MEP) and the fluctuations of HbO activity. However, when further investigating the relationship between PAS effects on task-related HbO/HbR changes (estimated using the HbO ratio, HbR respectively, calculated as the post- over pre-intervention amplitudes) and its effects on M1 excitability (estimated using the ratio of MEP), we also found no significant correlation. Therefore, it seems essential to carefully take into account intrinsic variability of both cortical excitabilities elicited by non-invasive brain stimulation and hemodynamic responses to tasks, when investigating the correlation between both effects.

To conduct accurate and robust investigations of PAS elicited cortical excitability (measured using MEP) and hemodynamic responses to finger tapping task (measured using HbO/HbR), we propose to study the variability of data within a hierarchical Bayesian model to infer PAS effects on both cortical excitability and hemodynamic response, as well as their correlation. Hierarchical Bayesian modeling allows taking into account heterogeneity of the variables of interest (MEP, HbO/HbR) at every stage (inter-/intra-subject, intervention type) of the analysis (Papaspiliopoulos et al., 2007; Betancourt and Girolami, 2015). Moreover, when considering a hierarchical structure, partial pooling can reduce the uncertainty of estimated parameters (Gelman et al., 2013; McElreath, 2020). This means that the group-level and individual-level estimations could inform each other to regularize the uncertainty of each parameter. In this context, Bayesian data analysis allows estimating the statistical expectation of each parameter of the model by sampling the joint posterior distributions. Thanks to the developments in Bayesian data analysis workflow during the last decade, Bayesian inferences have become more accessible and can provide accurate and reliable estimations of the posterior distribution. For instance, the most recent implementations of the Hamiltonian Monte Carlo (HMC) algorithm (Duane et al., 1987) called the dynamic HMC (Betancourt,

2017, 2019) is available as an open-source Bayesian statistical modeling and computation platform called Stan (Stan Development Team, 2020a). This technique not only accurately and efficiently samples the joint posterior distribution, but also provides robust estimations by quantitatively diagnosing pathological behaviors of Markov Chain Monte Carlo (MCMC) chains that are used to sample the joint posterior distributions (Betancourt and Girolami, 2015; Betancourt, 2017).

Considering the above advantages of the Bayesian approach, in this study, we applied a Bayesian data analysis workflow (Gabry et al., 2019; Gelman et al., 2020b) on our TMS/fNIRS dataset rather than the conventional analysis conducted in Cai et al., 2021b, to further investigate the relationship between the PAS effects task-related hemodynamic responses and its effects on M1 excitability. We hypothesize that enhanced brain excitability should be associated with higher hemodynamic activity elicited by a finger tapping task, and decreased excitability should be associated with a reduced hemodynamic response to the task. We first summarized the study design and data acquisition. Data preprocessing was then conducted to prepare the inputs of our Bayesian framework. We evaluated the relevance of three hierarchical models to investigate: 1) PAS effects on M1 excitability measured using MEP; 2) PAS effects on the whole-time course of task-related hemodynamic responses measured using fNIRS, and 3) the correlation between PAS modulated excitability changes and PAS modulated hemodynamic changes. The variability of each measurement was carefully considered in each model and at each level (i.e., at the individual and group levels) to conduct reliable estimations of the intervention effects and correlations. Statistical inferences were made via posterior predictive simulations (McElreath, 2020). Diagnostic of the models were conducted to ensure the robustness of the estimated posterior distributions.

2 Material and methods

2.1 Study design and subjects

Nineteen subjects (19 – 35 years old, male and right-handed) with no history of neurological disorders and no medications acting on the central nervous system were selected to participate in the study. We only included male participants in order to minimize the confounding of cortical excitability changes due to the menstrual cycle (Hattemer et al., 2007; Lee et al., 2017). This study was approved by the Central Committee of Research Ethics of the Minister of Health and Social Services Research Ethics Board (CCER), Québec, Canada. All subjects signed written informed consent prior to participation. They also

underwent a screening procedure to confirm no contraindications to MRI or TMS (Rossi et al., 2009; Suppa et al., 2017). Subjects were instructed to have a regular sleep cycle for the days and not to take caffeine for at least 90 minutes before the data acquisition.

The experiment paradigm of this study is illustrated in Fig.1.a. To modulate M1 cortical excitability and for inducing brain plasticity, three different intervention sessions were performed at least two days apart to minimize carryover effects. Each session consisted of five time-ordered sections, defined as follows:

1) ***A block designed finger-tapping task composed of 20 blocks, 10s of finger-tapping followed by 30s ~ 60s of resting was conducted within each block.*** Subjects were informed to tap their left thumb to the other 4 digits sequentially around 2Hz (Fig.1.a1). This long-range jitter was designed to prevent the task responses from phase locking to the undergoing physiological hemodynamic oscillations (Aarabi et al., 2017), therefore, reducing the physiological confounding on the task-related response at the stage of experiment paradigm design. Tapping onsets/offsets were instructed by auditory cues.

2) ***An event-related designed single pulse TMS (spTMS) composed of 75 events, jittered from 5s to 25s (Fig.1.a2).*** TMS procedures were performed with neuronavigation (Brainsight neuro-navigation system - Rogue-Research Inc, Canada) and based on subject specific anatomical MRI. TMS was delivered with a figure-8 coil (Magstim double 70mm remote control coil) connected to a Magstim 200^2 stimulator (Magstim Company, U.K.). In order to target M1, the coil was placed tangentially to the scalp and with a 45° angle to the midline of the head (Fig.1.c), so to maximize stimulation efficiency (Thomson et al., 2013). The individual 'hot spot' was defined for each session as the location with the largest Motor Evoked Potentials (MEPs) amplitude measured on the left thumb (Abductor Pollicis Brevis, APB) using electromyography (EMG). Stimulation intensity was set to 120% of the resting motor threshold (RMT), defined according to the maximum-likelihood parameter estimation by sequential testing approach (Awiszus et al., 1999; Ah Sen et al., 2017) using MTAT 2.0 (http://www.clinicalresearcher.org/software.html). All TMS procedures followed the recommendations of the International Federation of Clinical Neurophysiology (Rossi et al., 2009) and no participants reported any considerable discomfort or side effects.

3) ***A PAS session attempted to modulate the M1 cortical excitability (Fig.1.a3).*** PAS intervention consisted either in PAS25, PAS10 or sham-PAS. PAS was conducted with

100 pairs of electrical median nerve stimulation (MNS) on the left wrist, followed by TMS pulse delivered over the right M1, with a fixed interval of 10s between paired stimulations, for a total intervention of 18 minutes, as suggested in Suppa et al., (2017). MNS was delivered with a Digitimer (Digitimer DS7A, U.K) at the left median nerve and with the intensity equals 300% of the subject-specific perceptual threshold. TMS intensity was the same as the spTMS - 120% of RMT. After estimating subject-specific N20 response to electrical MNS using bipolar electroencephalogram (EEG) (BrainAmp ExG, Brain Products GmbH, Germany) on CP3 and CP4 electrodes, the interstimulus intervals (ISI) between MNS and TMS were determined to be pre-measured individual N20+5ms for PAS25 and N20-5ms for PAS10 (Carson and Kennedy, 2013). Sham parameters (e.g., MNS intensity, coil position, ISI) were the same as PAS25, but TMS was not delivered, and instead, its sound ('TMS click') was played via a stereo speaker.

4) ***Repetition of the event-related designed spTMS (Fig.1.a4) after the intervention.*** By comparing the MEPs measured during pre-intervention and post-intervention sessions, PAS intervention effects on M1 cortical excitability could be assessed.

5) ***Repetition of the block designed finger tapping task (Fig.1.a5) after the intervention***. Similarly, the corresponding effects on task-evoked hemodynamic responses could be estimated by comparing HbO/HbR concentration changes measured during pre-intervention and post-intervention sessions.

2.2 Data acquisitions

2.2.1 Anatomical MRI

Individual anatomical MRI was acquired to guide TMS and to calculate the head model required for fNIRS acquisition planning and fNIRS reconstructions. A General Electric Discovery MR750 3T scanner at the PERFORM Center of Concordia University, Montréal, Canada, was used to scan: 1) T1-weighted images using the 3D BRAVO sequence ($1 \times 1 \times 1$ mm^3, 192 axial slices, 256×256 matrix) and 2) T2-weighted images using the 3D Cube T2 sequence ($1 \times 1 \times 1$ mm^3 voxels, 168 sagittal slices, 256×256 matrix).

2.2.2 Motor Evoked Potentials

MEPs induced by spTMS pulses were measured to assess the M1 cortical excitability. A BrainAmp ExG bipolar system (BrainAmp ExG, Brain Products GmbH, Germany) was used to record EMG of the right abductor pollicis brevis (APB) muscle, with 2 TECA disposable

20mm disk electromyography (EMG) electrodes attached with a standard belly-tendon montage (Fig1.c).

2.2.3 Functional Near-Infrared Spectroscopy

fNIRS data were acquired to estimate the finger-tapping evoked hemodynamic responses (i.e., HbO/HbR). fNIRS data were acquired at 10Hz using a Brainsight fNIRS system (Rogue-Research Inc, Canada), which consists of two wavelengths – 685nm and 830nm. fNIRS optodes were placed to the subject's scalp using a clinical adhesive called collodion (Fig.1.c) to reduce motion artifacts (Yücel et al., 2014; Pellegrino et al., 2016; Machado et al., 2018) and to ensure a better contact with the skin when compared to standard fNIRS caps. A personalized optimal montage developed by our group (Machado et al., 2014, 2018; Pellegrino et al., 2016; Cai et al., 2021c) was used to maximize the sensitivity of fNIRS channels to a predefined region of interest (ROI) - the individual 'hand knob' region (see Fig.1.b) manually defined along the right M1 cortical surface which controls the left hand movement (Raffin et al., 2015). The resulted personalized optimal montage consisted of 3 sources and 15 detectors (see Fig.1.b). The distance between each source-detector pair was constrained to range from 2.0 cm to 4.5 cm. Each source was positioned to construct at least 13 channels among the 15 detectors ensuring a high spatial overlap between channels, to allow accurate local reconstruction along the cortical surface. A proximity detector was added at the center of 3 sources to record the physiological hemodynamics fluctuations within the scalp. Brainsight neuro-navigation system coregistered with subject specific T1 MRI was used to guide the installation and to digitize the position of fNIRS sources and detectors glued at their optimal positions. Additional 150 points were digitized on the head surface to allow accurate montage registration with the anatomical MRI, as a prerequisite for computing the fNIRS forward model. fNIRS data were acquired continuously during the whole experimental session, as described in Fig.1.a.

From the nineteen subjects selected for this study, one was excluded due to low sensitivity to TMS and two were excluded because they exhibited poor fNIRS signal qualities. Four subjects dropped out after the first session due to personal reasons, resulting in 16 PAS25, 12 PAS10 and 12 sham sessions. Please note that starting from here, we will denote 1) ***"Session"*** as one specific acquisition, consisted in any PAS intervention type, of one subject including experiments 1 to 5 as illustrated in Fig.1.a (e.g., PAS25 for Sub01); ***"Run"*** as one specific experiment (spTMS or finger tapping), before or after any PAS intervention type, of one subject (e.g., pre-PAS25 spTMS for Sub01); and ***"Time"*** to differentiate whether one

specific experiment was conducted before or after the intervention (e.g., pre-PAS25 vs. post-PAS25).

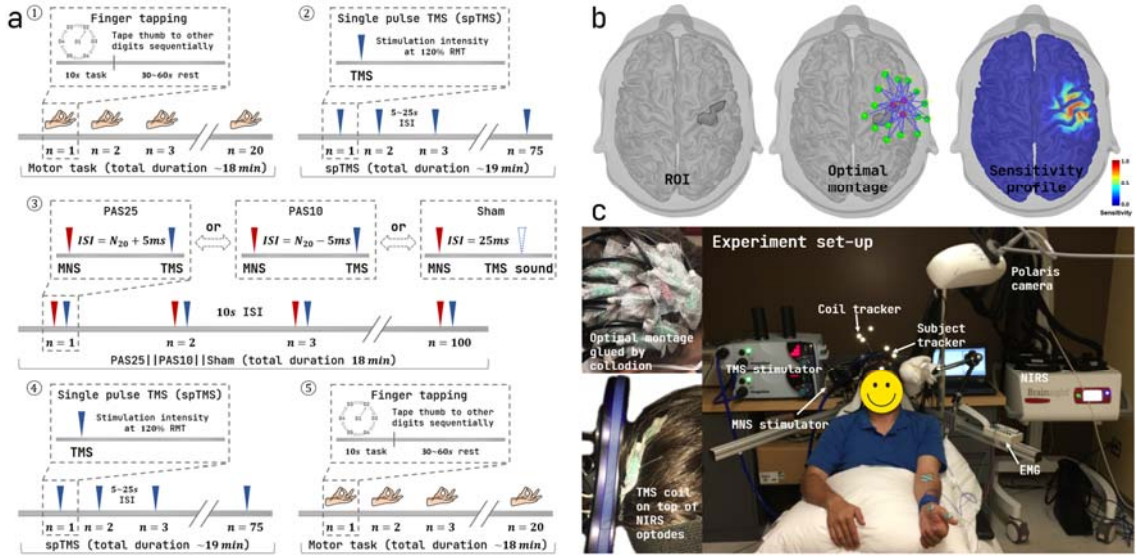

Fig.1. Experimental paradigm and set-up. *a) experiment paradigm ordered by time: 1) is a block designed finger-tapping task consisted of 20 blocks, each contained 10s task and 30s to 60s rest; subjects were informed to tapping their left thumb to the other 4 digits sequentially at around 2Hz; 2) is an event-related designed single pulse TMS (spTMS) run consisted of 75 events jittered from 5s to 25s. 3) PAS25/PAS10/sham-PAS consisted of 100 pairs of stimulations, interleaved by 10s; 4) and 5) repeated 2) and 1), respectively, after the PAS intervention. b) personalized optimal montage for fNIRS acquisition. 3 sources (red dots) and 15 detectors (green dots) were selected to optimize the sensitivity of fNIRS montage to a predefined ROI, the right M1 hand knob (outlined using a black profile) along the cortical surface. c) an overview of the experimental set-up, the personalized optimal montage was glued on the scalp using clinical adhesive – collodion; TMS coil was placed on top of the fNIRS optodes to target the 'hot spot' which corresponded to subject's left thumb, note that the low-profile feature of the fNIRS optodes allowed less TMS intensity decreases when departing from the scalp surface; a neuro-navigation system was used to guild the placement of the TMS coil and the digitization of the fNIRS optodes.*

2.3 Data preprocessing

2.3.1 EMG data processing

EMG data collected during spTMS runs were processed using Brainstorm software (Tadel et al., 2011) (https://neuroimage.usc.edu/brainstorm/) to extract MEP amplitudes. Raw EMG data were first band-pass filtered between 3 and 2000Hz. A time window from -10ms to 100ms around the stimulation onset was defined to extract MEP trials. These trials were then

baseline corrected (-10ms to 0ms), and the peak-to-peak amplitude of each MEP trial was calculated. Note that throughout the analysis reported in this study, none of the single MEP trials was excluded to preserve the intrinsic variability of MEP peak-to-peak amplitude measures. Hereby, for convenience, we will denote as "MEP", the actual MEP peak-to-peak amplitude, as often considered in TMS literature.

The output of the whole EMG data preprocessing section was a set of 75 MEPs estimated for each participant (specified by subject ID from 1 to 16), each intervention (PAS25, PAS10 or sham) and time (pre-PAS or post-PAS).

2.3.2 fNIRS data processing

fNIRS data processing was performed using the open-source fNIRS processing plugin - NIRSTORM (https://github.com/Nirstorm/nirstorm) implemented in our lab in Brainstorm software (Tadel et al., 2011) (https://neuroimage.usc.edu/brainstorm/). Raw fNIRS data were first preprocessed following standard recommendations (Yücel et al., 2020) and then converted to optical density changes (i.e., ΔOD). For each task run, 20 ΔOD epochs were extracted within a time window ranging from -10s to 30s around task onsets. To reduce motion artifacts and obtain the distribution of averaged ΔOD epochs for each run, we sub-averaged 16 out of 20 ΔOD epochs for all possible unique combinations (i.e., $C_{20}^{16} = 4845$ possibilities) and selected 50 of these sub-averaged ΔOD epochs below and above the median of the signal to noise ratio (SNR). To obtain the distribution of spatiotemporal map of HbO/HbR responses for each finger-tapping run along the cortical surface, we applied 3D fNIRS reconstruction workflow (Cai et al., 2021c) using personalized optimal montage and maximum entropy on the mean (MEM) to these 101 sub-averaged ΔODs. HbO/HbR spatiotemporal maps of each subject during each finger-tapping run (e.g., 101 HbO maps for Sub01 during pre-PAS25 finger-tapping) were co-registered to the mid-surface of the MNI ICBM152 template (Fonov et al., 2009, 2011), using FreeSurfer spherical transformation. An ROI was defined along the template surface as the "hand knob", to cover the cortical regions that control finger tapping. Finally, reconstructed HbO/HbR time courses (0s to 30s) within this "hand knob" ROI were averaged to represent the hemodynamic responses of each specific finger-tapping run. The output of the whole fNIRS data preprocessing section was a set of 80 runs (i.e., 40 sessions (16 PAS25+12 PAS10+12 sham) × 2 times) of 101 reconstructed HbO/HbR time course, for each run specified by subject (ID 1 to 16), intervention (PAS25, PAS10 or sham) and time (pre-PAS or post-PAS). Please see further details of fNIRS data processing in Appendix 1 and our previous study (Cai et al., 2021b).

2.4 Hierarchical Bayesian Modeling

To clarify the notation used in the following model equations, we used small letters to denote a scalar variable (e.g., μ for the mean of a Gaussian distribution) and capital letters to denote a matrix (e.g., Σ for the covariance matrix of a multivariate Gaussian distribution). A list of scalar values from one specific variable is represented by a small letter along with a subscript letter, for instance, a symbol μ_s refers to a list of means, and the subscript s represents each individual element of this list (mean for the sth session). The dimensionality of each list is given by the range of s (e.g., $s = 1, 2, 3, \ldots 40, for\ s^{th}\ session$). If subscript letter(s) is contained in square brackets, it means that the individual element of this list variable is differentiated by the model using index variables. Such as, i in $intercept_{[i=1,2,3]}$ indicates our model differentiates the intercept parameter for each intervention type by index variable $i = 1,2,3$, 1 for PAS25, 2 for PAS10 and 3 for sham.

2.4.1 Hierarchical Bayesian Model #1: Assessment of PAS effects on cortical excitability

We proposed a hierarchical Bayesian model to assess PAS effects on M1 cortical excitability, which was evaluated using the MEPs measured during spTMS runs before (pre-) and after (post-) each PAS intervention. This model consists of two parts: 1) a measurement error model taking into account the variability of MEPs within each spTMS run and 2) a multivariate hierarchical model describing post-intervention MEP as a linear function of pre-intervention MEP.

1) A model of measurement error

We assume the "empirical" mean of the observed MEP in each run to be drawn from a Gaussian distribution with the mean equals to the 'true' MEP amplitude and the scale equals to the standard error of all MEPs trials. The 'true' and observed ('obs') MEP of the pre-PAS spTMS run can be expressed as follows,

$$\begin{aligned} MEP_{obs,s}^{pre} &\sim \mathcal{N}ormal\left(MEP_{true,s}^{pre},\ MEP_{se,s}^{pre}\right) \\ MEP_{true,s}^{pre} &\sim \mathcal{N}ormal(0.5, 1) \\ s &= 1, 2, 3, \ldots 40, for\ s^{th} session \end{aligned} \tag{1}$$

where $MEP_{true,s}^{pre}$ is the 'true' value of the pre-PAS mean MEP for session s. $MEP_{obs,s}^{pre}$ is the "empirical" mean of the observed MEP from the same run expressed as,

$$MEP_{obs,s}^{pre} = \frac{\sum_{k=1}^{N} MEP_{k,s}^{pre}}{N} \quad k = 1, 2, 3, \ldots 75, for\ k^{th}\ trial \tag{2}$$

where $MEP_{k,s}^{pre}$ represents the pre-PAS MEP of the kth trial from a total of N=75 trials in session s. The corresponding measurement error $MEP_{se,s}^{pre}$ is then represented by the standard error of the MEP among all 75 trials, estimated by,

$$MEP_{se,s}^{pre} = \sqrt{\frac{\sum_{k=1}^{N}\left(MEP_{k,s}^{pre} - MEP_{obs,s}^{pre}\right)^2}{N(N-1)}} \tag{3}$$

Finally, substituting (2) and (3) into (1), both empirical mean and variance estimated over the 75 observed pre-PAS MEPs of a specific session were modeled to estimate the 'true' corresponding amplitude. For the prior distribution of $MEP_{true,s}^{pre}$, we applied a weakly informed prior (Gelman et al., 2008, 2017; Gabry et al., 2019) consisting in a Gaussian distribution $\mathcal{N}ormal(0.5, 1)$. Note that all observed MEPs ($MEP_{obs,s}^{pre,post}$ and $MEP_{se,s}^{pre,post}$, for 40 $Sessions \times 2\ Times\ (pre-/post-PAS) = 80$) were normalized by the global maximum value of $MEP_{obs,s}^{pre,post}$ to ensure a $[0, 1]$ range. Then, 0.5 appears as an appropriate prior of the mean when nothing is known about the MEP amplitude, but only the range (i.e., $(0+1)/2 = 0.5$).

The 'true' MEP in the post-PAS spTMS run was then modeled as follows,

$$\begin{aligned} MEP_{obs,s}^{post} &\sim \mathcal{N}ormal\left(MEP_{true,s}^{post}, MEP_{se,s}^{post}\right) \\ MEP_{obs,s}^{post} &= \frac{\sum_{k=1}^{N} MEP_{k,s}^{post}}{N} \\ MEP_{se,s}^{post} &= \sqrt{\frac{\sum_{k=1}^{N}\left(MEP_{k,s}^{post} - MEP_{obs,s}^{post}\right)^2}{N(N-1)}} \end{aligned} \tag{4}$$

Note that the prior distribution of the parameter $MEP_{true,s}^{post}$ is defined in the next section, within the context of hierarchical multivariate linear regression.

2) Hierarchical multivariate linear regression

PAS effects on M1 cortical excitability were then modeled using a multivariate linear regression model, in which $MEP_{true,s}^{post}$ and $MEP_{true,s}^{pre}$ were considered as the dependent and predictor variables, respectively.

$$
\begin{gathered}
MEP_{true,s}^{post} \sim \mathcal{N}ormal(\mu_s, \sigma) \\
\mu_s = intercept_{[i]} + \left(group_{[i]} + actor_{[a,i]}\right) \cdot MEP_{true,s}^{pre} \\
i = 1, 2\ and\ 3, for\ i^{th}\ intervention \\
a = 1, 2, 3, \ldots\ 16, for\ a^{th}\ subject \\
s = 1, 2, 3, \ldots 40, for\ s^{th}\ session
\end{gathered}
\tag{5}
$$

where μ_s is the mean of $MEP_{true,s}^{post}$, predicted by $MEP_{true,s}^{pre}$ using the following linear model: $\mu_s = intercept_{[i]} + \left(group_{[i]} + actor_{[a,i]}\right) \cdot MEP_{true,s}^{pre}$, and σ is the error of the linear regression (i.e., the scale of the normal distribution). We added the following index variables to differentiate subject, intervention (PAS25/PAS10/sham) and time (pre-/post-PAS) in the model. $intercept_{[i]}$ is the intercept of the linear regression, for the $i^{th}\ intervention$, in which $i = 1, 2\ and\ 3$ refers to PAS25, PAS10 and sham, respectively. The slope parameter is modeled using two parts, a group-level slope parameter $group_{[i]}$, specific for each intervention i, and a parameter modeling inter-subject variability, denoted as $actor_{[a,i]}$, for each intervention i and each subject a, associated with the following prior model:

$$
\begin{aligned}
&\begin{bmatrix} actor_{[a,i=1]} \\ actor_{[a,i=2]} \\ actor_{[a,i=3]} \end{bmatrix} \sim \mathcal{M}ulti\mathcal{N}ormal\left(\begin{bmatrix} 0 \\ 0 \\ 0 \end{bmatrix}, \Sigma\right) \\
&\Sigma = \Sigma_{actor} \cdot Rho \cdot \Sigma_{actor} \\
&\quad = \begin{pmatrix} \sigma_1 & 0 & 0 \\ 0 & \sigma_2 & 0 \\ 0 & 0 & \sigma_3 \end{pmatrix} \begin{pmatrix} 1 & \rho_{12} & \rho_{13} \\ \rho_{21} & 1 & \rho_{23} \\ \rho_{31} & \rho_{32} & 1 \end{pmatrix} \begin{pmatrix} \sigma_1 & 0 & 0 \\ 0 & \sigma_2 & 0 \\ 0 & 0 & \sigma_3 \end{pmatrix}
\end{aligned}
\tag{6}
$$

where $\mathcal{M}ulti\mathcal{N}ormal(\cdot)$ is a multivariate Gaussian distribution to model the interaction, which allows the effects of each specific intervention to vary for each subject, meaning each subject can respond to each intervention differently. We defined this multivariate Gaussian prior distribution to have zero means (3 elements vector) therefore assuming all the subjects to have zero mean deviation around the group-level slope parameter $group_{[i]}$. Rho and Σ_{actor} denote respectively the correlation matrix and the scale matrix of the covariance matrix Σ of the multivariate Gaussian distribution. $\sigma_{1,2,3}$ is the scale among all subjects within

each intervention group, for example, σ_3 is the scale of the vector $actor_{[a,i=3]}$ for sham. ρ is the correlation between pair-wised interventions, for instance, ρ_{12} represents the correlation between $actor_{[a,i=1]}$ for PAS25 and $actor_{[a,i=2]}$ for PAS10.

Weakly informed priors were assigned to the parameters in (5) and (6) as follows,

$$\begin{gathered} intercept_{[i]} \sim \mathcal{N}ormal(0, 0.1) \\ group_{[i]} \sim log\mathcal{N}ormal(log(1), 0.5) \\ \rho \sim \mathcal{LKJ}corr(2) \\ \sigma \sim \mathcal{H}alf\mathcal{N}ormal(0, 1) \end{gathered} \tag{7}$$

$\mathcal{N}ormal(0, 0.1)$ was chosen for $intercept_{[i]}$ considering that when $MEP_{true,s}^{pre} = 0$, the corresponding $MEP_{true,s}^{post}$ should not be too much apart from 0. $log\mathcal{N}ormal(log(1), 0.5)$ was selected for the group-level slope to ensure it is a positive value with a median of 1. Therefore, without knowing any intervention type, the slope should be equal to 1, assuming there is no averaged PAS effect among subjects when the intervention type is not known. $\mathcal{LKJ}corr(\eta = 2)$, the Lewandowski-Kurowicka-Joe distribution (Lewandowski et al., 2009), is a weakly informative prior for the correlation parameter ρ that does not prioritize extreme correlation values such as ± 1, where η is a positive parameter. $\eta = 1$ denotes uniform density of ρ. The larger η is (when compared to 1), the least likely the extreme correlation values to occur (sharper probability density distribution). We selected $\eta = 2$ as a weakly informed prior commonly considered in Bayesian data analysis (McElreath, 2020). Finally, $\mathcal{H}alf\mathcal{N}ormal(0,1)$ was used for variance parameters to ensure a positive value, whereas its likelihood decreased following the positive half of a $\mathcal{N}ormal(0, 1)$ distribution, when variance increases. As denoted previously, we normalized all data $MEP_{k,s}^{pre}$ and $MEP_{k,s}^{post}$ within the range [0,1], therefore $\mathcal{N}ormal(0, 1)$ is considered as a conservative ("flat") enough prior, not reducing the variance.

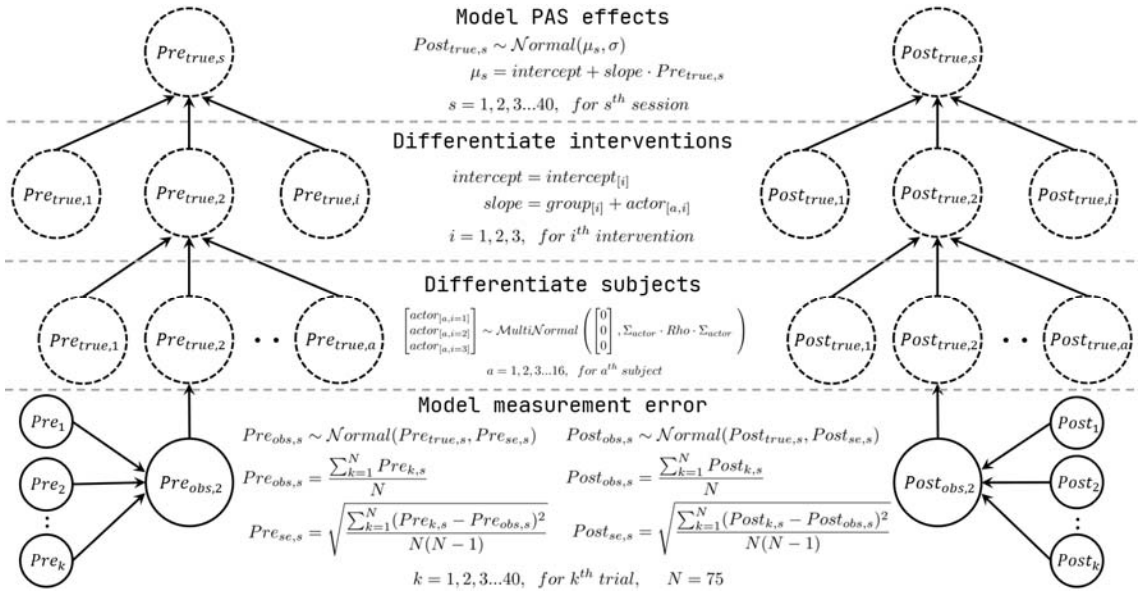

Fig.2. The hierarchical model of PAS effects on either cortical excitability (MEP) or hemodynamic responses (Hb). *From bottom to top, 1) a measurement error model assuming the mean of the variable of interest (either the observed MEPs, e.g.,* $MEP_{se,s}^{pre}$*; or a spline weight of HbO/HbR time course, e.g.,* $w_{obs,s,n}^{pre}$ *of each run at a different time (pre-/post-) is drawn from a Gaussian distribution. The mean of this Gaussian distribution is the 'true' value of the variable of interest, and the scale is the corresponding standard error; 2) each subject and intervention were differentiated using index variables; 3) PAS effects were modeled by linear regression in which the 'true' post-variable of interest was predicted by the 'true' pre- variable of interest. Solving this hierarchical model by Bayesian allows partial pooling on each parameter to reduce the uncertainty.*

2.4.2 Hierarchical Bayesian Model #2: Assessment of PAS effects on task-related HbO/HbR

A similar hierarchical multivariate linear regression model is proposed to assess PAS effects on task-related fNIRS hemodynamic responses. This model is very similar to previous Model#1, the main difference being that the input variables to the model are now 'features' representing hemodynamic responses during the finger-tapping task. Instead of extracting amplitudes at a particular time sample of HbO/HbR time courses, for instance, the hemodynamic peak amplitude, or performing a local average within a specific time window, in this Model #2, we conducted a procedure to model the PAS effects over the whole time course of HbO/HbR responses to finger tapping.

To do so, after 3D reconstruction using MEM of all 101 sub-averaged of the fNIRS responses, HbO/HbR time courses were first averaged within the selected M1 ROI in the

selected time range [0s, 30s]. To lower the dimension of the input to the model, resulting time courses were then projected on B-splines temporal basis functions (Boor, 2001; Gelman et al., 2013; Hastie, 2017). Therefore, hemodynamic responses were expressed as a weighted linear combination of those basis functions, considering the hierarchical model summarized in Fig.3. Please note that Hb refers to either HbO or HbR in the model, which was fitted separately for each chromophore,

$$
\begin{aligned}
Hb_{obs,s}^{pre}(t) &\sim \mathcal{N}ormal\left(\mu_s^{pre}(t),\ Hb_{sd,s}^{pre}(t)\right) \\
\mu_s^{pre}(t) &= w_{obs,s,n}^{pre} \times B_n(t) \\
w_{obs,s,n}^{pre} &\sim \mathcal{N}ormal(0,10) \\
Hb_{obs,s}^{post}(t) &\sim \mathcal{N}ormal\left(\mu_s^{post}(t),\ Hb_{sd,s}^{post}(t)\right) \\
\mu_s^{post}(t) &= w_{obs,s,n}^{post} \times B_n(t) \\
w_{obs,s,n}^{post} &\sim \mathcal{N}ormal(0,10) \\
n &= 1, 2, 3, \ldots\ 10, for\ n^{th}\ weight \\
t &= 0s\ to\ 30s\ with\ a\ step\ of\ 0.5s \\
s &= 1, 2, 3, \ldots 40, for\ s^{th}\ session
\end{aligned}
\tag{8}
$$

where $Hb_{obs,s}^{pre}(t)$ is the observed empirical mean of pre-PAS HbO/HbR responses among all 101 sub-averaged time courses, for a specific finger-tapping run (e.g., finger-tapping run in pre-PAS25 of Sub01) of a specific session s at a specific time point t. $Hb_{obs,s}^{pre}(t)$ is assumed to follow a Gaussian distribution with a mean of $\mu_s^{pre}(t)$ and a scale of $Hb_{sd,s}^{pre}(t)$, where $Hb_{sd,s}^{pre}(t)$ is the corresponding standard deviation estimated among all 101 sub-averaged time courses. Note that all pre- and post-PAS HbO/HbR time courses in one session were normalized by the global maximum amplitude to be within the range [-1,1]. Then, $\mu_s^{pre}(t)$ representing the mean time course of the true pre-PAS HbR/HbO for time sample t and session s , was defined as a linear combination of $n = 10$ B-spline basis functions $B_n(t)$ using the corresponding weight $w_{obs,s,n}^{pre}$. Each basis function $B_n(t)$ was defined as a 3rd order polynomial function. A similar model structure was applied to data and parameters corresponding to the post-PAS finger-tapping run. To model the temporal response using B-spline, we selected 10 knots pivoted at the percentiles of time sequence $t = 0s\ to\ 30s$ with a step of $0.5s$; therefore, 10 corresponding weights and basis functions, as illustrated in the second column of Fig.3. Using this Bayesian spline model, not only the averaged time course of HbO/HbR, but also their corresponding standard deviation over the 101 sub-averaged, for

each time point, were projected in the 'spline space'. This means the averaged time course of HbO/HbR can be recovered by the linear combination of the mean of each weight (over 101 sub-averaged) and basis functions $B_n(t)$, whereas the standard deviation of HbO/HbR time course is reflected by the linear combination of the standard deviation of each weight (over 101 sub-averaged) and $B_n(t)$. Note that the use of spline basis functions in this study was mainly to reduce the dimensionality of the HbO/HbR time course from 60 sampling points to 10 weights, while preserving the variability structure to be modeled. Therefore, selecting 10 spline knots was a trade-off between: 1) choosing fewer knots that would result in eventual distortion of the HbO/HbR time courses, involving too much temporal smoothness; 2) adding more knots that would increase the dimensionality of the data after projection. Hence, our empirical choice ensured accurate representation of the whole HbO/HbR time courses with a minimum dimensionality span. Importantly, projecting to spline space also preserved the autocorrelation of the HbO/HbR time courses per se, which could not be achieved when simply applying the same hierarchical model on each of 60 data points independently. Finally, $\mathcal{N}ormal(0,10)$ is considered as a weakly informative prior for spline weight considering the HbO/HbR time course was normalized within the range [-1,1].

We then embedded this spline model of the hemodynamic response within the same hierarchical model proposed in the previous section (Model#1), for instance, replacing the $MEP_{obs,s}^{pre}$ with the spline weights $w_{obs,s,n}^{pre}$ as follows, also illustrated in the third column of Fig.3.

$$\begin{aligned} w_{obs,s,n}^{post} &\sim \mathcal{N}ormal\left(w_{true,s,n}^{post}, w_{sd,s,n}^{post}\right) \\ w_{obs,s,n}^{pre} &\sim \mathcal{N}ormal\left(w_{true,s,n}^{pre}, w_{sd,s,n}^{pre}\right) \\ w_{true,s,n}^{post} &\sim \mathcal{N}ormal(\mu_s, \sigma) \\ \mu_s &= intercept_{[i]} + \left(group_{[i]} + actor_{[a,i]}\right) \cdot w_{true,s,n}^{pre} \\ w_{true,s,n}^{pre} &\sim \mathcal{N}ormal(0,10) \end{aligned} \tag{9}$$

where $w_{obs,s,n}^{post}$ $w_{obs,s,n}^{pre}$,$w_{sd,s,n}^{post}$ and $w_{sd,s,n}^{pre}$ were all calculated from the corresponding posterior of spline weights estimated from equation (8). In total, 10 models were considered for 10 pairs of weights (pre- and post-PAS) to encode the PAS effects for either HbO or HbR separately. $w_{obs,s,n}^{post}$ and $w_{obs,s,n}^{pre}$ are referring to the empirical mean of each spline weight for either pre- or post-PAS HbO/HbR for session s, estimated from the corresponding posterior of spline weights in equation (8). The scale of Gaussian distribution in the measurement error

model was then $w_{sd,s,n}^{post}$ and $w_{sd,s,n}^{pre}$, respectively. Note that equation (8) resulted in the estimated posterior distribution of $w_{obs,s,n}^{post}$ and $w_{obs,s,n}^{pre}$ after projecting HbO or HbR time course to the spline space, then scales of Gaussian distributions used for the measurement error model in (9) were directly reflected by the standard deviation of the posterior distribution (denoted as sd in subscript). Finally, the intervention, subject index variables, and priors to be considered for this model, were similar to those previously introduced for Model#1, so the PAS effects on HbO/HbR whole time course were then encapsulated in the hierarchical model of spline weights.

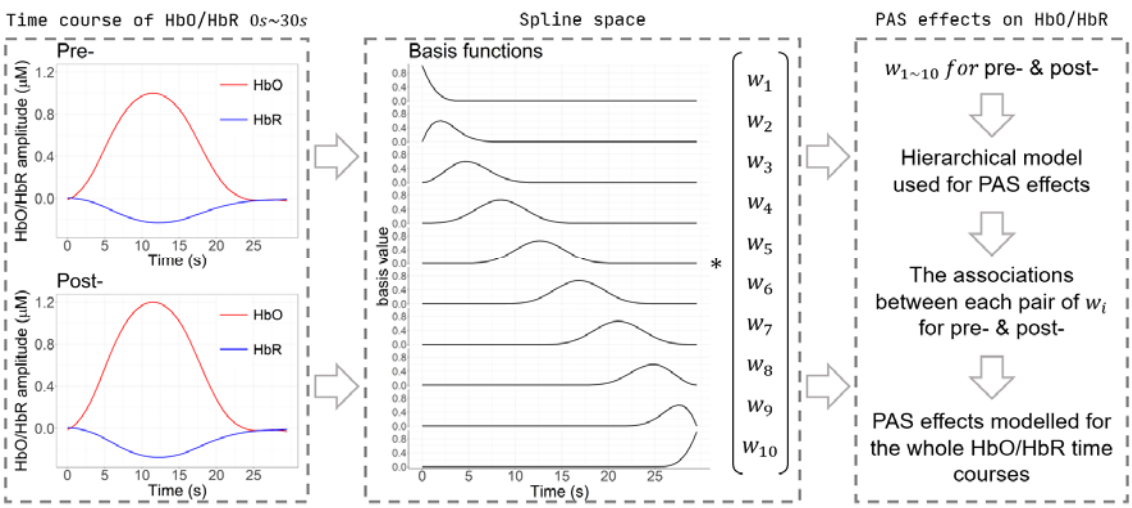

Fig.3. The hierarchical model for PAS effects on the whole HbO/HbR time course. *HbO/HbR time courses, from 0s to 30s, before and after each intervention session were selected as the inputs of the model. They were projected into the spline space which is composed of 10 predefined basis functions (3rd order polynomial with 10 knots). The linear combination of basis function using 10 corresponding weights* $w_{1\sim10}$ *can fully recover the HbO/HbR time course. The resulting pre- and post-PAS spline weights were then fed into the hierarchical model, similar to model #1 to estimate the PAS effects on each weight. Therefore, the associations between each pair of weights encapsulated the PAS effects on the whole time course of HbO/HbR.*

2.4.3 Hierarchical Bayesian Model #3: Relationship between PAS effects on task-related M1 hemodynamic activity and PAS effects on M1 excitability

In this third model, we propose to investigate the interactions between 1) PAS effects on M1 excitability (PAS effects on MEP, represented by the slope parameter in Model#1), and 2) PAS effects on reconstructed hemodynamic finger tapping responses (PAS effects on HbO/HbR, represented by the slope parameter in Model#2 for a specific weight w_n). We

assumed the relationship between task-related M1 hemodynamic activity and M1 excitability was not intervention specific, then the previous hierarchical models (i.e., Model#1 and Model#2) were modified to be only session specific, i.e., only index variable of session s was used, whereas intervention and subject index i and a were ignored.

$$\begin{bmatrix} slope_{[s]}^{MEP} \\ slope_{[s]}^{Hb} \end{bmatrix} \sim \mathcal{M}ulti\mathcal{N}ormal\left(\begin{bmatrix} 0 \\ 0 \end{bmatrix}, \Sigma_{slope}\right)$$

$$\begin{aligned} \Sigma_{slope} &= \Sigma_{session} \cdot Rho_{slope} \cdot \Sigma_{session} \\ &= \begin{pmatrix} \sigma_{MEP} & 0 \\ 0 & \sigma_{Hb} \end{pmatrix} \begin{pmatrix} 1 & \rho_{MEP-Hb} \\ \rho_{Hb-MEP} & 1 \end{pmatrix} \begin{pmatrix} \sigma_{MEP} & 0 \\ 0 & \sigma_{Hb} \end{pmatrix} \\ s &= 1, 2, 3, \ldots 40, for\ s^{th}\ session \end{aligned} \tag{10}$$

The interactions were modeled using a multinormal distribution, in which the parameter ρ_{MEP-Hb} in the Rho_{slope} matrix denotes the correlation between the two slopes (representing the PAS effects in both linear models). The same model was fitted separately when investigating either the relationship between MEP and HbO or between MEP and HbR. $slope_{[s]}^{MEP}$ is the session specific slope parameter in Model#1. Similarly, $slope_{[s]}^{Hb}$ (either HbO or HbR) is the session specific slope parameter in Model#2 for one of the corresponding spline weights $w_{1\sim10}$. σ_{MEP} and σ_{Hb} are the standard deviations of $slope_{[s]}^{MEP}$ or $slope_{[s]}^{Hb}$, respectively. Note that this model was fitted for each spline weight separately - 10 correlation investigations between MEP and each spline weight were conducted. Therefore, the posterior distribution ρ_{MEP-Hb} inferred for a specific spline weight can be interpreted as the correlation between brain excitability and task-related cortical hemodynamic activity at a specific period (e.g., w_5 reflecting HbO/HbR fluctuations around the peak time point of the hemodynamic response). For the parameters of the Multinormal distribution, we considered the same weakly informed priors as those proposed in Model#1 and Model#2.

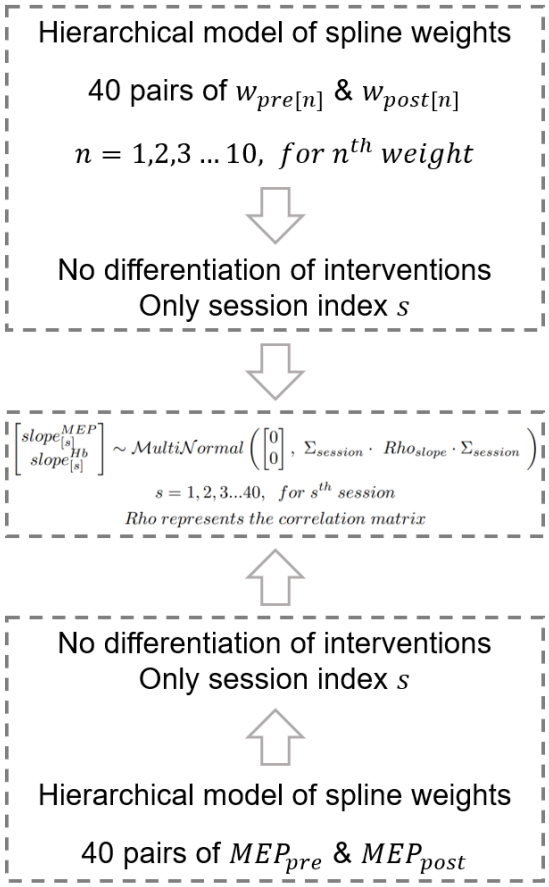

Fig.4. Modeling the relationship of task-related M1 hemodynamic activity and M1 excitability. *For MEP, which represented the M1 excitability, the previous Model #1 was modified to be session-specific only. For spline weights, which represented the features of task-related HbO/HbR time course, the previous 'Model #2 was also modified to be session-specific only. The association between the* $slope_{MEP}$ *in MEP model and* $slope_{Hb}$ *represented by any of the spline weight of the HbO/HbR time course model were described by a multinormal distribution.*

2.5 Prior predictive simulation

To justify the choices of 'weakly informed' prior, a prior predictive simulation was conducted in Fig.3. The prior predictive simulation consists in a generative process simply checking what kind of data we would expect to generate from our hierarchical models, when applying all possible values of the parameters considering the proposed prior distributions of the model. Then by comparing the distribution of data generated by our model, to the domain knowledge, one can assess whether the proposed priors could be overregulating or not objective (e.g., too strongly informed). In our study, PAS effects were modeled using linear regression. To perform prior predictive simulation, we considered prior predictive simulation to draw 1000 lines following the prior distributions of the intercept and slope in the

normalized pre-MEP vs. post-MEP amplitude plane. Then the distribution of generated regression lines was compared to three reference lines summarizing our knowledge of the problem. In detail, these three reference lines were featuring a slope of 0.2, 1 and 3, respectively and an intercept of 0. When the intercept is set to 0, the slope just refers to the ratio of post- over pre-PAS MEP amplitude, which was used in conventional analysis to represent the PAS effects. Whereas a slope of 1 would then correspond to no effect (post-/pre-PAS ratio of 1), the reference slopes of 0.2 and 3 represented the thresholds for outliers of extremely small or large MEP ratios reported in Kriváneková et al., 2013.

2.6 Hierarchical Bayesian model fitting

In this study, we used the R Version 4.0.3 (R Core Team, 2020) distribution of the Stan Probabilistic programming languages (Stan Development Team, 2020a) - RStan package Version 2.21.2 (Stan Development Team, 2020b) to implement and solve the proposed Bayesian models. Specifically, the joint posterior distribution was sampled using the implementation of dynamic HMC in Stan (Betancourt, 2017, 2019), as an improved version of HMC algorithm (Neal, 2010; Betancourt and Girolami, 2015). In total, 4 MCMC chains were used to sample each model and they were initialized randomly to ensure a better exploration of the joint posterior distribution, while allowing diagnostic of the convergence. Each chain consisted of 2000 samples, including a first half warm-up phase (1000 samples) for the adaptation of the HMC parameters. Therefore, when combining all 4 chains, we obtained 4000 samples of each parameter of the models mentioned above, drawn respectively to estimate the corresponding posterior distributions. Regarding computation time, using an Intel 10750H laptop CPU and parallel computation (one core per chain), dynamic HMC took 66s for sampling once Model#1, 59s for Model#2 and 53s for Model#3 (including compiling time and calculation of the diagnostics).

Diagnosing the HMC sampling process is a crucial step when evaluating the accuracy and biases of the estimated posterior distributions. This is also known as a unique and advanced feature of HMC when compared to other MCMC algorithms (Roberts and Rosenthal, 2004). In this study, we considered the diagnostic approach recommended by Stan to evaluate pathological behaviors of HMC sampling (Betancourt, 2017; Gabry et al., 2019; Gelman et al., 2020b),

1) ***Divergent transitions for real samples drawn after the warm-up phase.*** This diagnostic statistic is specific for the HMC sampler, mainly invigilating the miss-match between the

step size of the MCMC chain and the target distribution geometries (Betancourt et al., 2017). While sampling a 'high curvature' region of the target distribution, an inappropriate large step size may miss-sample it, therefore biasing the resulted posterior distribution. MCMC chains will approach infinite energy immediately – called divergent transitions – when approaching such regions (Neal, 2010; Betancourt, 2017). These divergences are recorded and reported by Stan. Note that divergence is usually related to the parameterization of the model, especially when involving multivariate and hierarchical structures. Parameters may usually be dependent on each other in these models, therefore, creating a 'high curvature' distribution landscape, also denoted as Neal's Funnel (Neal, 2003), which is difficult to sample. In order to reduce the chances of such divergences, in our study, we considered reparameterization of the model into non-centered forms when sampling with HMC.

2) ***The Energy-Bayesian Fraction of Missing Information (E-BFMI) is a specific diagnostic statistic for HMC sampler, evaluating the efficiency of the sampling process*** (Betancourt, 2016). Poorly chosen parameters of the HMC can decrease the efficiency of the sampling process or even result in incomplete exploration of the target distribution, especially when considering distributions with heavy tails. Such a behavior can be diagnosed by taking advantage of the physics feature of HMC, by comparing the marginal energy density (denoted as π_E) and energy transition density (denoted as $\pi_{\Delta E}$) of the chain. When superimposing the histograms of π_E and $\pi_{\Delta E}$, the higher the efficiency, the more overlap between the two distributions. The Energy Bayesian Fraction of Missing Information (E-BFMI) (Rubin, 2004) is used in Stan to quantify such comparison, by calculating the statistical expectation of the variance of $\pi_{\Delta E}$ over the variance of π_E. Empirically, an E-BFMI value below 0.3 is considered as problematic (Betancourt, 2016, 2017).

3) ***$\hat{R}$ as a general and primary diagnostic statistic when evaluating convergence of MCMC chains*** (Gelman and Rubin, 1992; Brooks and Gelman, 1998). $\hat{R}$ is estimated for each parameter of the model as the ratio of between-chains variance over the within-chain variance. In detail, the between-chains variance is calculated as the standard deviation among all chains, whereas the within-chain variance is calculated as the weighted sum of the root mean square of the standard deviation within each single chain. The recommended criteria for convergence is $\hat{R} < 1.05$ (Gabry et al., 2019; Vehtari et al., 2020).

Finally, we used tidyverse package (Wickham et al., 2019) in R (R Core Team, 2020) for general data wrangling and visualization. Tidybayes package (Kay, 2020) was used for visualizing the posterior distributions whereas bayesplot package (Gabry et al., 2019; Gabry and Mahr, 2020) was used for visualizing the diagnostics of HMC chains.

2.7 Statistical inferences

In general, two types of statistical inferences were made in this study. To infer PAS effects on MEP and HbO/HbR time course, we applied the posterior predictive simulation technique in which the distribution of MEP after each intervention type was estimated by feeding the fitted model (e.g., Model#1 and Model#2) with specific pre-intervention MEP values (the same approach was applied to HbO or HbR time course, respectively). Then the distribution of percentage change of post-intervention MEP relative to pre-intervention MEP was used to infer the PAS effects on MEP (the same approach was applied to HbO or HbR time course, respectively). To infer the correlation between PAS effects on MEP and its effects on HbO/HbR, we directly considered the posterior distribution of the correlation parameter in Model#3. Please find further details as follows.

1) When investigating the effect of PAS on MEP, we first made inferences by answering the question - what will be the distribution of MEP after a certain PAS intervention when giving a specific pre-PAS MEP? This approach is more direct and convenient comparing the process checking the posterior distribution of each parameter of the model one by one. This technique is referred to as the posterior predictive simulation (Gabry et al., 2019; Gelman et al., 2020b). For instance, ***to infer the PAS effects on the M1 cortical excitability,*** we used the averaged MEP (i.e., equals to 1.0mV, in the original data scale before normalizing) among all pre-PAS runs to represent the group-level pre-PAS M1 cortical excitability. This amplitude was then substituted into the fitted Model#1 along with all posterior distributions of parameters (e.g., intervention-specific intercepts and slopes) to estimate a group-level post-PAS MEP distribution. By comparing the distributions of the percentage change of this post-PAS MEP distribution relative to the pre-PAS MEP amplitude, the effects of each intervention can be inferred. We also performed this inference using a set of different pre-PAS MEPs values, such as 0.2mV, 0.6mV, 1.2mV, 2.2mV and 2.8mV according to the observed range of all individual pre-PAS MEP (i.e., ranging from 0.1mV to 3.0mV), to investigate how PAS effects could be related to the pre-PAS MEP amplitude. Note that these pre-PAS MEP amplitudes were

also scaled by dividing the global maximum value of $MEP_{obs,s}^{pre,post}$ before being feed into the model, and posterior predicted post-PAS MEP amplitudes were rescaled back to the original data scale.

Similarly, ***the PAS effects on task-related hemodynamic*** were statistically inferred using the following steps: 1) select any preferred pre-PAS HbO/HbR time course (e.g., the averaged HbO/HbR of all pre-PAS runs demonstrated in the results); 2) calculate the 10 weights (variable) corresponding to this specific time courses; 3) inferring the 10 post-weights along with their variance by posterior predictive simulations of the fitted hierarchical Model#2; 4) apply a linear combination of 10 post-weight and basis functions to obtain the distribution of post-PAS HbO/HbR time course. Note that we also calculated the PAS effects on HbO/HbR by contrasting post-PAS25 or post-PAS10 hemodynamic response to the one obtained in post-sham condition. To do so, we subtracted from the posterior predicted distributions of post-PAS25 HbO/HbR time courses (or post-PAS10) the posterior predicted post-sham HbO/HbR time courses.

2) ***The correlation between M1 cortical excitability and task-related hemodynamic response*** can be inferred directly from the posterior distribution of the correlation parameter ρ_{MEP-Hb} per se. Note that this correlation distribution was estimated for each spline weight separately, therefore, the resulted posteriors can be used to infer the excitability association for each specific time point of the HbO/HbR time course. For instance, the posterior distribution of the correlation between $slope_{[s]}^{MEP}$ and $slope_{[s]}^{Hb(w_5)}$ indicated the relationship between the peak period (e.g., few seconds around the expected peak timing of the response) of task-related HbO/HbR and M1 cortical excitability. We also conducted typical frequentist inferences of this relationship using the linear fit and Pearson's correlation over all 40 sessions on the resulted mean of $slope_{[s]}^{MEP}$ and $slope_{[s]}^{Hb(w_5)}$, for both HbO and HbR.

Note that for quantified statistics, we reported median and the median absolute deviation (i.e., mad_{sd}), which was suggested by Gelman et al., 2020a and estimated as follows: $mad_{sd} = 1.483 \cdot median_{i=1}^{n} |z_i - M|$, where z_i is a certain value of a set of values $z_{i=1,2,3...n}$ and M is the median of all z_i. The mad_{sd} is a more universal representation of the variance, which is comparable to the standard deviation, without considering the parametric/nonparametric distribution of z_i and is more computationally stable.

2. 8 Data and code availability statements

The original raw data supporting the findings of this study are available upon reasonable request to the corresponding authors. fNIRS and TMS data were processed via Brainstorm software (Tadel et al., 2011) available at https://neuroimage.usc.edu/brainstorm/ and the fNIRS processing plugin - NIRSTORM (https://github.com/Nirstorm/nirstorm) in Brainstorm. R code for Bayesian models is available upon reasonable request to the corresponding authors.

3. Results

3.1 Prior predictive simulation

As illustrated in Fig.5, the resulting prior predictive simulation lines were distributed symmetrically around the control line suggesting no PAS effect (i.e., intercept = 0, slope =1). This means our priors exhibited no preference towards a slope < 1 or >1. Moreover, within the post-PAS MEP versus pre-PAS MEP plane, the area spanned by all simulated lines covered a larger area than the area enfolded by the reference lines (0 intercepts, a slope spanning from 0.2 to 3.0). These results are confirming that priors in our hierarchical model are not biased to the expected PAS effect and are more conservative than the conventional MEP ratio thresholding approach. This prior predictive simulation result also applies to PAS effects on HbO/HbR, since fNIRS data were normalized similarly as MEP values and the priors in the multivariate linear regression models were the same.

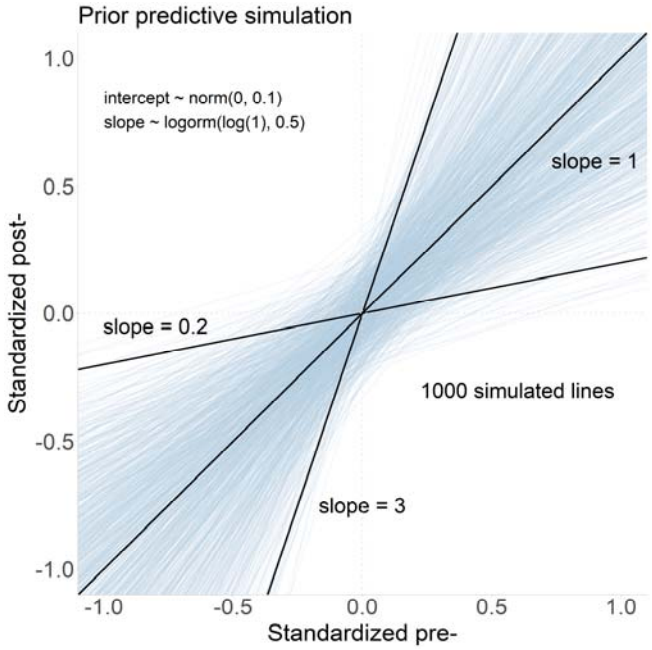

Fig.5. Prior predictive simulations for the hierarchical model of PAS effects on cortical excitability. *Each blue line represents one prior predictive simulation obtained by drawing simultaneously the intercept and the slope parameters when considering only the priors proposed in Model#1. For comparison purposes, as a reference, we first represented a control line suggesting no PAS effect (intercept of 0, slope of 1), then two lines referring to MEP ratio outliers (intercept of 0 and slope of 0.2 and 3 respectively.*

3.2 Diagnosis of HMC

All of the models resulted in 0 divergences reported by Stan, indicating they were well parameterized, and HMC chains explored sufficiently well the target distribution. Fig.6 reports the evaluation of diagnostic statistics for the two metrics $\hat{R}$ and E-BFMI. In each column of Fig.6, a specific model sampling process for a specific model is being diagnosed (see further details in Fig.6 caption). The first row illustrates the histogram of $\hat{R}$ for all parameters in each corresponding model. No parameters resulted $\hat{R} > 1.05$ indicating the corresponding HMC chains indeed well converge. The second row demonstrated the superimposed histograms of π_E (i.e., marginal energy density) and $\pi_{\Delta E}$ (i.e., energy transition density), which overlapped well for all models. This evaluation was also quantified by reporting E-BFMI values for each model, which were all smaller than 0.3. Therefore, we can conclude that the HMC chains used to sample the parameters of the key models involved in this study were robust and reliable according to these reported diagnostic statistics.

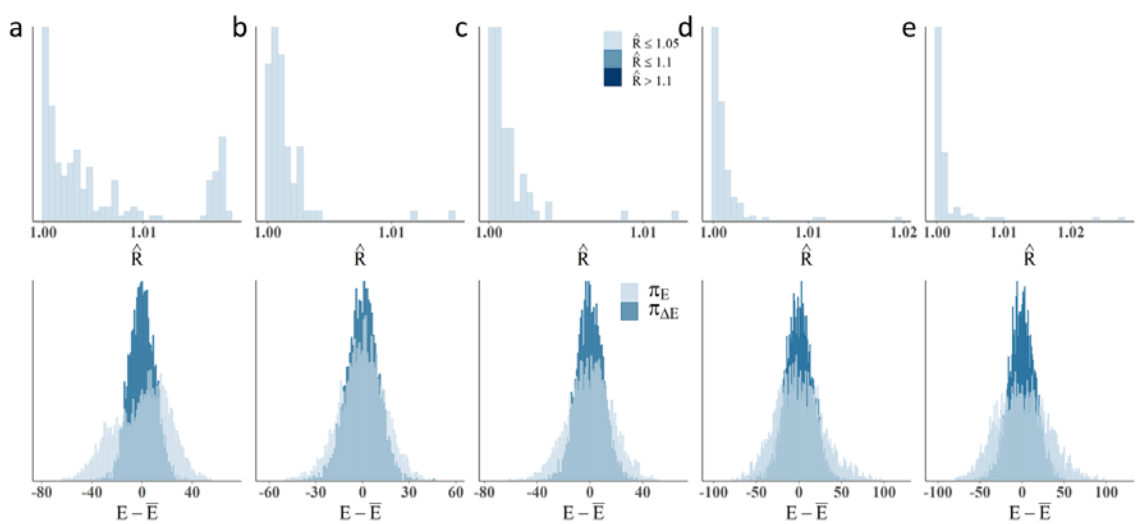

Fig.6. Diagnostic statistics of key features of the models considered in this study*. Diagnostic statistics for a) Model#1 - PAS effects on MEP amplitude, b) Model#2 - PAS effects on w_5 of task-evoked HbO, c) Model#2 - PAS effects on w_5 of task-evoked HbR, d) Model#3 - correlation between*

PAS effects on MEP and PAS effects on w_5 of task-evoked HbO and e) Model#3 - correlation between PAS effects on MEP and PAS effects on w_5 of task-evoked HbR. The first row presents the histogram of $\hat{R}$ values for all parameters among all chains of each model. No $\hat{R}$ value was above 1.05, suggesting that all chains converged well. The second row presents the superimposed distributions of the marginal energy density π_E and the energy transition density $\pi_{\Delta E}$ for all HMC chains sampled for each model. The corresponding quantification metric E-BFMI was smaller than 0.3, indicating a good overlapping between the two distributions.

3.3 PAS effects on cortical excitability

When considering Model#1, the estimated regression lines (using the averaged intercept and slope parameters calculated from their posterior distributions) linking pre- and post-PAS MEPs for each intervention are reported in Fig.7a. The regression line estimated for sham intervention (black line) was found as expected - between the regression lines estimated for PAS25 (red line) and PAS10 (blue line), and it was almost identical to the reference line reporting no effect (intercept=0, slope=1). Observed pairs of post-PAS MEP and pre-PAS MEP mean amplitude over all trials are presented as solid pints (observed data), whereas corresponding estimated 'true' amplitudes are presented as empty points. The black lines connecting each pair of solid (observed mean) and empty (estimated 'true' mean) points illustrate the shrinkage process, also known as the result of partial pooling obtained when considering hierarchical Bayesian modeling. This demonstrated the regularization property of the model, where the estimated 'true' MEPs corresponding to each intervention group shrank toward the corresponding regression line. Moreover, when considering the variance of the MEPs, the larger the MEP variability of a certain run, the more shrinkage there was. Results of posterior predictive simulation at the group-level, when considering a pre-PAS MEP amplitude of 1.0mV is illustrated in Fig.7b, as the posterior distribution of relative changes of post-PAS MEP amplitudes (in %) after each intervention. PAS25 intervention resulted in a substantial relative increase of post-PAS MEP amplitude (median $\pm mad_{sd}$ = $30.6\% \pm 14.6\%$), consisting of a posterior probability of 0.97 for obtaining an increase in MEP amplitude. The posterior distribution of sham post-PAS MEP amplitude exhibits a nice symmetric pattern around a 0% increase (an increase of $2.3\% \pm 14.5\%$). The effects of PAS10 were subtle, showing a slight shift towards the negative side consisting in a relative decrease of $-1.80\% \pm 11.0\%$, and a probability of 0.57 of obtaining a decrease in MEP amplitude. Individual-level inferences are presented in Fig.S1, where both PAS25 and PAS10 effects are showing a large between-subject variability, as addressed in the introduction.

When reporting individual level results, posterior predictive simulations were obtained by considering the same averaged pre-PAS MEP amplitude over 40 sessions as the input for all subjects, taking full benefit of hierarchical modeling, allowing to compare individual-level results within the appropriate framework.

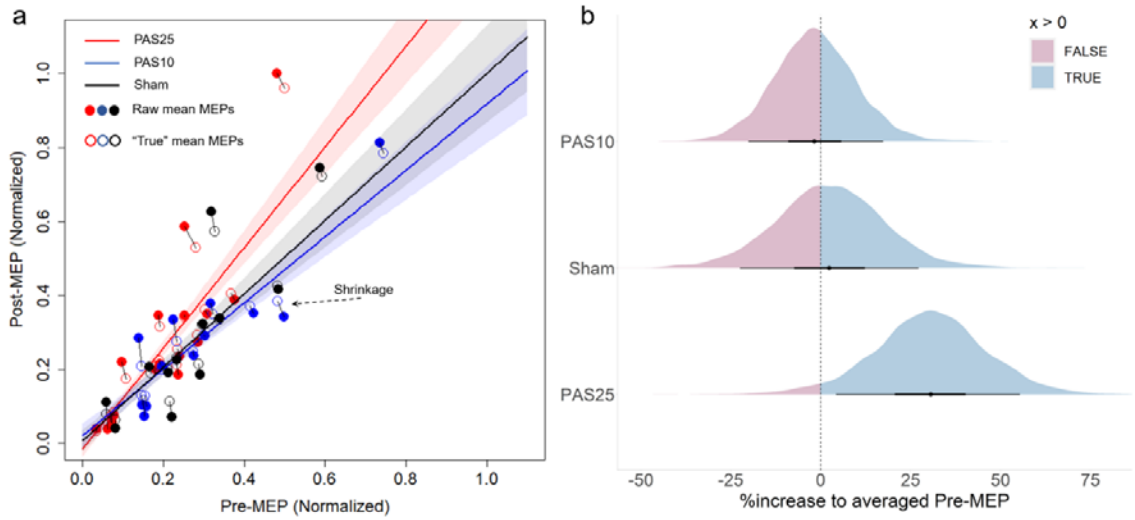

Fig.7. PAS effects on cortical excitability*. a) the regression lines of each intervention estimated by the mean of intercept and slope from the corresponding posterior distribution, PAS25 (red), PAS10 (blue) and sham (black). Pre- and post-PAS MEP amplitudes were normalized by dividing by the global maximum amplitude of all 80 MEP values. Shadow areas represent the 50% interval estimated from the posterior distribution of the regression parameters. Solid points correspond to pairs of averaged pre-/post-PAS MEP amplitudes over all trials of each specific run. Empty points represent the 'true' amplitude of the corresponding pre-/post-PAS MEP pair estimated using the proposed hierarchical Bayesian Model#1. The black bar connecting each solid point to the corresponding empty point illustrates the shrinkage process of Bayesian inference of the hierarchical model; b) Posterior predictive simulations of post-PAS MEP amplitudes obtained when considering a given pre-PAS MEP amplitude of 1mV as input, corresponding to the averaged pre-PAS MEP amplitude over all 40 sessions. The blue area represents the probability of obtaining a relative increase (in %) for the post-PAS MEP amplitude when compared to the pre-PAS MEP amplitude, whereas the pink area represents the probability of obtaining a relative decrease (in %). The black dot represents the median of each posterior distribution, and the surrounding bars show the corresponding 50% and 90% credibility intervals.*

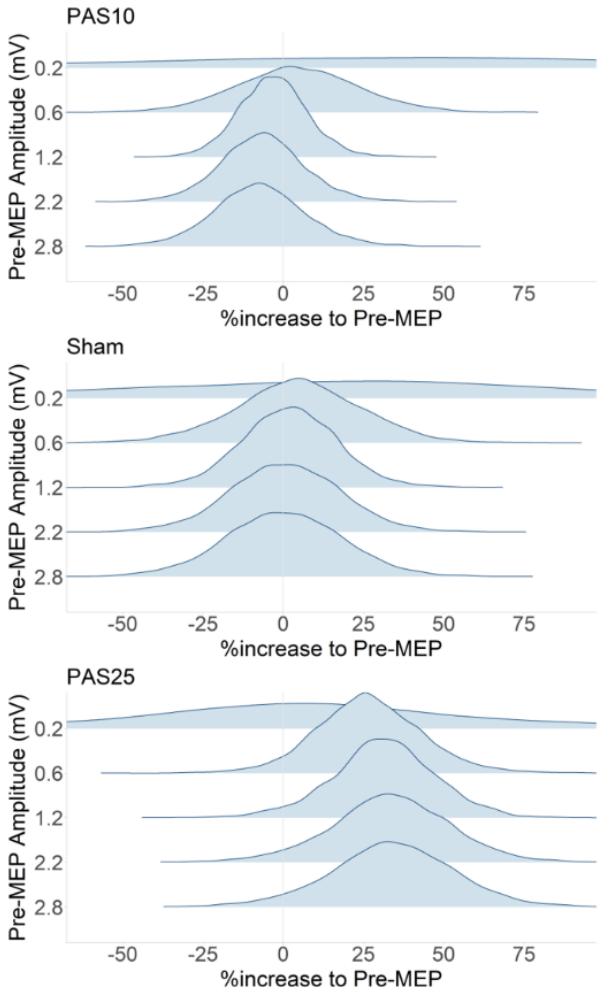

Fig.8. Effects of spTMS intensity on PAS assessment. *We used posterior predicting simulations applied to five levels of pre-PAS MEP amplitudes, to evaluate the impact of five levels spTMS intensities. Posterior distributions of the corresponding relative changes in post-PAS MEP amplitude relative to pre-PAS MEP amplitudes are presented in each row. The expected effects of PAS25 (positive % increase) and PAS10 (negative % decrease) became clearer when increasing the spTMS intensity. On the other hand, when considering the sham intervention, we found no effect of relative changes in post-PAS MEP amplitude, exhibited at all intensity levels, as well as symmetric distributions around 0%.*

Fig.8 presents the effects of simulating different pre-PAS MEP amplitudes as inputs, on the relative change of post-PAS MEP amplitude for each intervention, at the group level. For both PAS25 and PAS10, the higher the pre-PAS MEP amplitude was, the higher the relative change in MEP amplitude was. In further details, PAS25 resulted in an increase of post-PAS MEP amplitude of ( ), ( ), ( ) and ( ) when considering

an input pre-PAS MEP amplitude of 0.6mV, 1.2mV, 2.2mV and 2.8mV, respectively. Similarly, PAS10 resulted in an increase of post-PAS MEP amplitude of $+4.2\% \pm 18.9\%$ ($Prob = 0.59$), when considering an input pre-PAS MEP amplitude of 0.6mV, followed respectively by decreases of $-3.1\% \pm 10.5\%$ ($Prob = 0.62$), $-6.5\% \pm 12.6\%$ ($Prob = 0.70$) and $-7.51\% \pm 13.8\%$ ($Prob = 0.71$) when considering an input pre-PAS MEP amplitude of 1.2mV, 2.2mV and 2.8mV. This important finding of our proposed Bayesian Model#1 suggests that even without increasing the TMS stimulation intensity during PAS, simply increasing the spTMS intensity considered to measure changes in excitability can reveal the expected PAS effects more clearly, while reducing some variability in the data. On the other hand, when assessing this effect on sham, we obtained similar distributions of relative changes in post-PAS MEP amplitude, all symmetric around 0%, consisting in relative changes of 4.6%, 2.0%, 0.6% and 0.2% , when considering a pre-PAS MEP amplitude of 0.6mV, 1.2mV, 2.2mV and 2.8mV, respectively. Importantly, the higher the pre-PAS MEP amplitude was, the closer to 0% the median of relative change in post-PAS MEP amplitude was. Overall, when considering pre-PAS MEP amplitude of 0.2mV for each intervention, we found a large level of uncertainty in spTMS responses, suggesting that small MEP amplitude induced by spTMS should be avoided when assessing the level of brain excitability.

3.4 PAS effects on task-related HbO/HbR responses

Fig.9 showed the PAS effects on the whole time course HbO/HbR, as a contrast (i.e., subtraction of posterior distributions) between the intervention of interest (PAS25 or PAS10) and sham condition. When considering the group level averaged pre-PAS HbO/HbR responses (normalized to [-1, 1]) as input for posterior predictive simulations (dashed red and blue curves for HbO and HbR), we observed that PAS25 (Fig.9a) resulted in a relative increase of HbO amplitude (solid red curve) and HbR amplitude (solid blue curve), mainly around the expected peak of the hemodynamic response (from 8s to 16s). When comparing absolute peak amplitudes, the probability of increasing the hemodynamic response after PAS25 was 0.80 for HbO response and 0.82 for HbR response. After PAS10 (Fig.9b), our results are suggesting at the group level a subtle relative decrease of HbO and HbR absolute amplitudes around the peak of the hemodynamic response. The probability of obtaining a relative decrease in absolute peak amplitudes after PAS10 was 0.66 for HbO response and 0.48 for HbR response. Interestingly, PAS10 demonstrated a clear absolute amplitude decrease within a period ranging from the peak to the end of the response (11s to 25s) for both HbO and HbR.

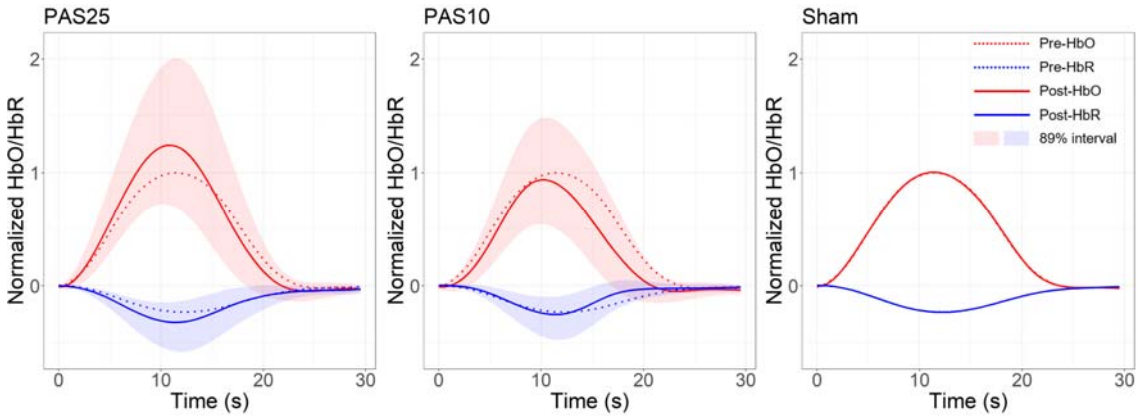

Fig.9. PAS effects on the whole time course of HbO/HbR. *Posterior predictive simulations of post-PAS HbO/HbR time course (solid curves: HbO in red and HbR in blue) when considering pre-PAS HbO/HbR template input defined as the group-level averaged pre-PAS HbO/HbR response (normalized to [-1,1]) over all 40 sessions (dash curves). The shadow area represents the 89% credibility interval of resulted post-PAS HbO/HbR responses. Note that sham effects were subtracted from the PAS25 and PAS10 to obtain so-called 'unbiased' effects. The overlappings of lines in the sham panel are shown as a sanity check of the contrast.*

3.5 Relationship between PAS effects on task-related cortical hemodynamic activity and PAS effects on M1 excitability

Fig.10a presents inferences on the relationship between PAS effects on task-related cortical hemodynamic activity and PAS effects on M1 excitability, represented by the posterior distribution of correlations between the slope of MEP amplitudes (post-PAS versus pre-PAS) and the slope of spline weight w_5 (post-PAS versus pre-PAS) for either HbO or HbR task-related responses. Since our previous observations of the PAS effects were conducted for the whole HbO/HbR time course (Fig.9), we selected w_5 as the spline weight of interest considering it corresponded to the spline basis function exhibiting a peak at 12.5s, therefore consisting in the closest temporal pattern when compared to the expected hemodynamic response. The probability of obtaining a positive correlation between PAS effects on MEP amplitude and PAS effects on HbO response was 0.77; and 0.79 for a positive correlation between PAS effects on MEP amplitude and PAS effects on HbR response. The corresponding 89% highest posterior density interval (HPDI) of this correlation was [-0.26, 0.89] for HbO; and [-0.20, 0.84] for HbR. Fig.10b presents the linear fits between the averaged $slope_{[s]}^{MEP}$ and the averaged $slope_{[s]}^{Hb(w_5)}$ obtained for each session s among all 40

sessions. The corresponding estimated Pearson's correlation was 0.58 for MEP vs. HbO ($p < .0001$, $CI_{95\%} = [0.33, 0.75]$) and 0.56 for MEP vs. HbR ($p < .001$, $CI_{95\%} = [0.30, 0.74]$).

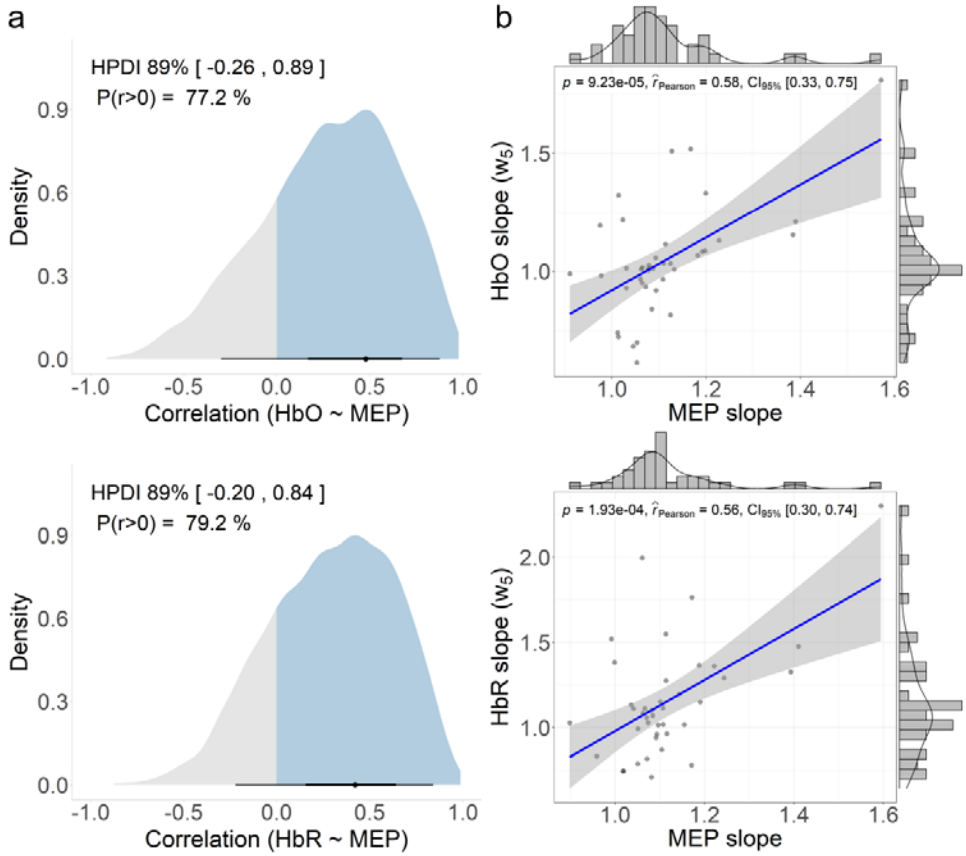

Fig.10. The relationship between task-related cortical hemodynamic activity and M1 excitability. *a) the posterior distribution of the correlation between* $slope_{[s]}^{MEP}$ *and* $slope_{[s]}^{Hb(w_5)}$ *for HbO (top) and HbR (bottom). The blue area represents the probability of observing a positive correlation (ρ>0). The black dot represents the median of each posterior distribution, and the surrounding bars show the corresponding 50% and 90% credibility intervals. b) Linear fit (blue line) between the averaged* $slope_{[s]}^{MEP}$ *and the averaged* $slope_{[s]}^{Hb(w_5)}$ *obtained for all 40 sessions (each represented by a grey dot). The grey area indicates the 95% confidence interval of the regression. Estimated Pearson's correlation between* $slope_{[s]}^{MEP}$ *and* $slope_{[s]}^{Hb(w_5)}$ *over the 40 sessions together with corresponding p-values and 95% confident intervals are shown on top of each panel. The marginal histograms and fitted density functions are shown on the side of each corresponding marginal axis.*

Fig.11 illustrates the posterior distribution of the correlation between $slope_{[s]}^{MEP}$ and $slope_{[s]}^{Hb(w_n)}$, when considering each spline weight for $n = 2,3,4,5,6,7\ and\ 8$. The closer the corresponding peak of the spline basis function associated with the weight w_n was to the

expected peak of the HbO/HbR response, the higher the correlation between and was. In further details, the median of these correlation values was respectively -0.05, 0.13, 0.28, 0.31, 0.13, -0.10 and 0.01 when considering for HbO; and a median value of 0.06, 0.17, 0.31, 0.32, 0.15, -0.06 and 0.03 when considering for HbR, therefore confirming this trend. Our results are suggesting that the expected positive correlation between PAS effects on task-related hemodynamic response and PAS effects on M1 excitability appeared mostly around the peak of HbO/HbR time course (e.g.,), in agreement with PAS effects reported previously in Fig.9. On the other hand, for the earliest aspects of the hemodynamic response (modeled using) as well as for the end of the response (modeled using), we found a posterior correlation with a median close to zero, suggesting no relationship between and for the corresponding time periods.

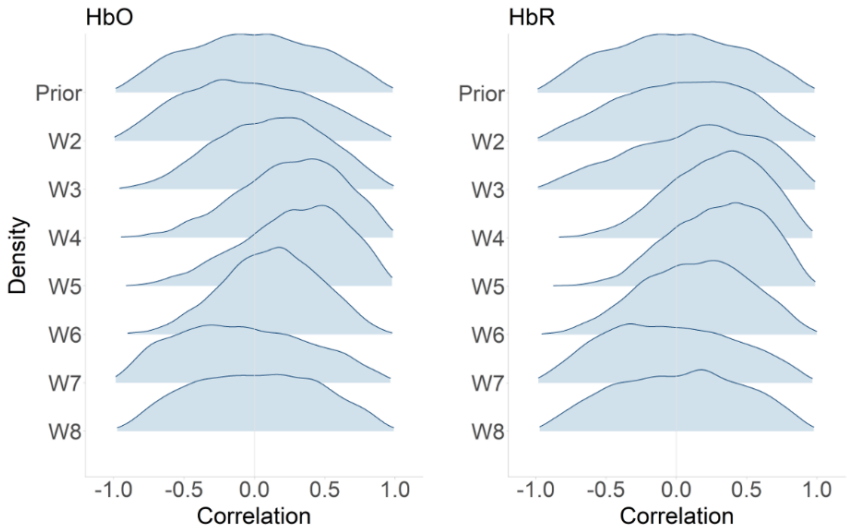

Fig.11. Posterior distributions of the correlations between and several selected . *The posterior distribution of the correlation between and , when considering each spline weights for for HbO (left) and for HbR (right). The prior distribution of the correlation (i.e., LKJ(2)) on the first row demonstrates a perfect symmetric to the 0 correlation. There was a trend showing the closer the corresponding peak of the spline basis function associated with the weight was to the expected peak of the HbO/HbR response, the higher the correlation between and was. showed the highest correlation values for both HbO and HbR as it corresponded to the spline basis function exhibiting the peak at 12.5s, therefore the closest temporal pattern when compared to the expected*

hemodynamic response. In contrast, the earliest aspects of the hemodynamic response (modeled using $w_{2,3}$) and the end of the response (modeled using $w_{7,8}$), showed almost identical distributions when comparing to the prior.

4. Discussion

4.1 PAS effects on cortical excitability

Using hierarchical Bayesian modeling, we first investigated PAS effects on cortical excitability, which was measured using MEP amplitude induced by spTMS. Probability distributions of the relative changes (in %) of post-PAS MEP amplitudes, when compared to pre-PAS MEP amplitudes, were estimated using posterior predictive simulations. Our results showed a substantial increase of MEP amplitude after PAS25, a subtle decrease after PAS10 and no changes after control (sham). These results are consistent with previous PAS studies (Stefan, 2000; Wolters et al., 2005; Tsang et al., 2015; Lee et al., 2017; Suppa et al., 2017). These studies considered conventional MEP analysis, calculating the ratio between the averaged MEP amplitude after PAS over the one before PAS. Therefore, when MEP ratio was larger than 1, it indicated an excitability increase and vice versa. In contrast, here we applied a full Bayesian workflow using an advanced sampling algorithm. The benefits of this procedure are: 1) multivariate linear regression allowed the differentiation of interventions and subjects, hence modeling the heterogeneity of intervention effects exhibited in different groups of data; 2) involving intercept in linear regression reduced the influences of low MEP amplitudes runs when compared to the conventional ratio calculation of post- over pre-PAS MEPs; 3) the variability of MEP amplitudes were considered in the estimation of the PAS effects rather than only using the averaged amplitudes of each run and ignore the variance; 4) parameters of the model were estimated by Bayesian inferences using dynamic HMC algorithm sampling posterior distributions using a hierarchical structure and weakly informed priors, therefore, allowing partial pooling to reduce the estimation uncertainty; 5) flexible and intuitive statistical inferences of the modeled PAS effects were obtained by conducting posterior predictive simulations from the model learned from the data. This means by giving any pre-PAS MEP amplitude and intervention index, the distribution of the corresponding group-level post-PAS MEP amplitude could be estimated; Finally, 6) the estimated PAS effects were reliable and informative, as suggested by their posterior probability distributions, rather than considering only a statistical significance test providing a dichotomous output.

Moreover, our model also allowed inferring the effects of MEP amplitude itself on the effect size of the resulted excitability changes modulated by PAS. In Fig.8, we reported a pattern suggesting that the higher the MEP amplitude was, the larger was the effect size of both PAS25 and PAS10. This pattern was not biased when comparing to the sham session, which showed no effects for different pre-PAS MEP amplitudes. It is important to mention that when considering posterior predictive simulation, the intensity of the TMS pulse during the intervention session (PAS25 or PAS10 or sham) did not change. This means the underlying intervention effects did not change. Then considering spTMS as the assessment procedure to measure brain excitability, our results are suggesting that a high enough spTMS intensity might help to measure more accurately PAS effects. Please also note that the pre-PAS MEP amplitudes (0.2mV, 0.6mV, 1.2mV, 2.2mV and 2.8mV) used in this posterior predictive simulation were selected based on the observed range (0.1mV to 3.0mV) of all individual pre-PAS MEP. This observed range of MEP from our data is also consistent with the spTMS evoked MEP distribution estimated by a recent meta-analysis study in which 687 health subjects' data were considered among 35 studies (Corp et al., 2021). More importantly, this meta-analysis study also investigated the relationship between the baseline MEP (referred to as the test stimulation) amplitude and the short interval intracortical inhibition (SICI) by polling data from 15 studies consisted of 295 healthy subjects. They showed a significant negative relationship between the baseline MEP amplitude and SICI, suggesting that "SICI is best probed by high relative test stimulation intensities" (Corp et al., 2021). This result is also concordant with our finding on PAS10, in which the higher the pre-PAS MEP (test stimulation) is, the more PAS10's inhibitory effects (decreased post-PAS MEP comparing to the pre-PAS MEP) are pronounced. This consistency demonstrated the power of our Bayesian analysis to infer similar findings from relatively small sample-sized data when comparing with meta-analysis results consisting of a much larger sample size.

4.2 PAS effects on the whole HbO/HbR time course of finger tapping responses

To our best knowledge, our study demonstrated for the first time PAS effects on the whole time course of task-related HbO/HbR time courses. In contrast, few time segments along selected time windows were considered in previous studies, then HbO or HbR amplitudes were just averaged within each time segment and compared before and after interventions (Chiang et al., 2007; Yamanaka et al., 2010). In our previous study (Cai et al., 2021b) we also simply averaged the HbO/HbR amplitude within a 5s long time window centered around the peak of the hemodynamic response to represent the total amount of hemoglobin delivered to

the region of interest. The Bayesian approach proposed in this study brings more insight into the investigation of PAS effects on hemodynamics, considering not only the peak amplitude before and after interventions, but whole HbO/HbR time courses. For instance, visual inspections of results presented in Fig.9 are suggesting that PAS effects are indeed more pronounced around the peak of the expected hemodynamic response. This is expected if we can assume that the hemodynamic response function (HRF) is not much affected by interventions, then the expected task-related hemodynamic response would result from a convolution with a higher or lower amplitude boxcar function representing excited or inhibited neuronal activity patterns (Sotero and Trujillo-Barreto, 2007). Therefore, the effect of intervention should appear mostly around the peak, and the closer to the peak the higher the effect size. Consequently, averaging HbO or HbR amplitude within a certain time window would 'dilute' the estimation of the effect of interest, especially when considering the effect size was not large, for instance around 25% increase for HbO after PAS25 is shown in Fig.9.

The fact that PAS intervention effects could be observed mainly around the peak of hemodynamic time courses may also explain the difficulty of investigating similar questions using fMRI. Indeed, a typical BOLD signal is sampled around 0.5Hz using standard fMRI sequences. Such low temporal resolution may not be sufficient to sample well the effects around the peak and could possibly explain why no PAS effects were found on BOLD signal changes in the PAS and fMRI study reported by Kriváneková et al., 2013. Besides, depending on how well fMRI BOLD samples and the actual peak of the hemodynamic response are phased-locked, the mismatch between the time of BOLD signal sampling and the actual peak of the response may introduce some confounds, when comparing BOLD signal changes before and after PAS interventions. Another benefit of modeling accurately the whole HbO/HbR time course is the possibility to offer alternative interpretations of PAS effects. For instance, our results in Fig.9 showed a slight time shift for HbO after PAS25 and a larger one after PAS10 (e.g., the peak time of HbO shifted from 12s to 10s after PAS10). The decrease of HbO amplitudes after PAS10 was also mainly exhibited from 11s to 25s of the response time courses. These observations may suggest a more complex mechanism of the effect of neuronal plasticity on neurovascular coupling. Further analysis using the deconvolution technique (Machado et al., 2021) to estimate HRFs that are related to these hemodynamic responses may help us to better investigate such a potential mechanism but it is beyond the scope of this study.

It is important to mention that we did not perform a specific analysis for every time sample of the hemodynamic response. We regularized and reduced the dimensionality of the problem by projecting HbO/HbR responses on B-splines as temporal basis functions. Therefore, PAS effects on hemodynamic were modeled by only 10 weights instead of 60 data points, whereas the actual post-PAS HbO/HbR time courses could then be fully retrieved from the estimated weights and the spline basis functions. The choice of the number and locations of knots might have limited the 'resolution' of our proposed correlation analysis. There are more advanced Bayesian spline approaches, such as the penalized spline (P-spline) (Eilers and Marx, 2010; Ventrucci and Rue, 2016), which introduces an extra prior to regularize the number of effective knots. This approach was mainly designed to smooth a time course and prevent overfitting rather than considering an accurate representation of the time course. Non-parametric time series modeling techniques were also proposed in this context, without assuming the location of the knots along the time course. For instance, Gaussian process regression (Neal, 1998) characterizes the time course, such as the hemodynamic response, as an unknown function. Samples of the time course are then drawn from a multinormal distribution providing a full covariance matrix of all time samples. Our analysis could benefit from these non-parametric approaches to avoid eventual limitations associated with the choice of the knots, but this was beyond the scope of this study.

It is also worth noting that these results of PAS effects on the whole HbO/HbR time courses were also benefiting from accurate time courses estimated by our previously proposed fNIRS reconstruction workflow (Cai et al., 2021c). In this workflow, the fNIRS acquisition montage was personalized and the detection sensitivity of it was maximized to the individual ROI. Meanwhile, the MEM framework adapted from our previous works in the context of electro-/magneto-encephalogram source imaging (Chowdhury et al., 2013, 2016; Grova et al., 2016; Heers et al., 2016; Hedrich et al., 2017; Pellegrino et al., 2020) for conducting fNIRS reconstruction (Cai et al., 2021a) also ensured accurate estimation of HbO/HbR time courses from reconstructed spatiotemporal maps. For instance, delays between HbO and HbR peak times were around 1s shown in Fig.9, which is consistent with our previous finding (Cai et al., 2021c) and fNIRS literature (Jasdzewski et al., 2003; Steinbrink et al., 2006).

4.3 Relationship between PAS effects on task-related hemodynamic and PAS effects on M1 excitability

We also investigated the relationship between PAS effects on task-related hemodynamic activity and PAS effects on cortical excitability along the whole HbO/HbR time course.

When compared to standard frequentist analysis of the correlation between $slope_{[s]}^{MEP}$ and $slope_{[s]}^{Hb(w_n)}$ reported in Fig.10b, our proposed Bayesian analysis was more informative since we could estimate the whole posterior distribution of such a correlation, instead of providing a single correlation value estimated from the mean effects while ignoring the variance. Even if the sample size was not large and we acknowledge the influences from large variability of PAS effects and variability of task-evoked hemodynamic responses, our proposed hierarchical Bayesian models were able to demonstrate a high probability of positive correlations between MEP and hemodynamic slopes (representing the PAS effects), around the peak of HbO and HbR responses. This finding is consistent with previous results reported in animal studies, suggesting a positive correlation between hemodynamic responses and cortical excitability. For instance, Allen et al., 2007 demonstrated decreased oxygenations in anesthetized cat's visual cortex after applying inhibitory rTMS; increased fMRI resting-state connectivity, GABA, glutamine and glutamate levels after performing excitatory rTMS. Reduced connectivity and glutamine levels after applying inhibitory rTMS on healthy rat's right hemisphere were reported by Seewoo et al., 2019. The reliability of our proposed model was further confirmed by the fact that no correlation was found between PAS effects on MEP and hemodynamic responses, when considering other time windows, such as the initial aspects and the end of the hemodynamic response. The further the analyzed time period was to the expected hemodynamic peak, the closer to the prior was to the posterior distribution of the correlation, with no preference on either positive or negative correlations.

4.4 HMC sampling and diagnostic

Taking advantage of dynamic HMC to sample the hierarchical Bayesian models in this study, we were able to carefully diagnose the pathological behavior of MCMC sampling chains (Betancourt, 2017, 2019). This diagnostic procedure is an essential step when applying Bayesian data analysis (Gelman et al., 2020b). To allow accurate and reliable inferences, MCMC chains must explore well the typical set of the posterior distributions, in which most of the probability density is contained. For instance, the convergence of MCMC chains needs to be confirmed and quantified to ensure such full explorations. When inappropriate parameters of the chain are chosen (e.g., the step size), abnormalities such as divergences should be detected to avoid eventual sampling biases. In our study, we reported several diagnostic statistics for all key components of three models using both visualization and quantified metrics, following the recommendations of the Stan team (Gelman et al., 2013;

Gabry et al., 2019; Stan Development Team, 2020a). The proposed diagnostic statistics considered here also constitute a unique feature of HMC sampling, when compared to conventional MCMC algorithms such as Gibbs sampling (Geman and Geman, 1984; Gelfand and Smith, 1990). HMC is also considered to be more accurate by taking advantage of sampling all parameters at the same time, comparing to Gibbs that often samples parameters alternatively one after the other which may bias the resulted posterior distribution due to the inherent correlations between parameters. Overall, the diagnostic analysis of the sampling process in this study is suggesting that our inferences are built upon well-sampled posterior distributions, reasonably accurate and unbiased. Similar HMC sampling and diagnostic approaches were also reported in several recent studies, such as a Bayesian virtual epileptic patient to model the spread of epileptic activity (Hashemi et al., 2020); a Bayesian latent spatial model for mapping biomarkers of the progression of Alzheimer's disease (Dai et al., 2021); the Bayesian multilevel modeling to improve statistical inferences in fMRI analysis (Chen et al., 2019b, 2019a, 2021) and a hierarchical Bayesian model to investigate mechanisms of reinforcement learning and decision-making (Ahn et al., 2017).

4.5 Limitations and perspectives

While the Bayesian approach is known to improve the uncertainty of statistical inferences when dealing with small samples data set, as illustrated by our results, there is no doubt that this study would benefit from a larger sampling size. Conventional frequentist power analyses (Bhalerao and Kadam, 2010) could estimate the minimum number of samples required to obtain a significant effect for a statistical power such as 80%. When considering the standard deviation of MEP amplitudes and fMRI BOLD signals reported in PAS (López-Alonso et al., 2014) and in fMRI literature (Kriváneková et al., 2013), we estimated that when assuming random sampling, at least 50 subjects would be required for MEP analysis and more than 100 subjects would be required for hemodynamic analysis using fMRI BOLD. Despite the inherent limitation of power analysis which may underestimate the sample size (Gelman and Carlin, 2014), in practice, it is challenging to conduct acquisitions with this amount of subjects especially considering all three different interventions.

We only involved one model for each investigation in this study. It is indeed recommended to construct multiple models based on different hypotheses of the same question and then quantitatively compare these models using techniques such as cross-validation to choose the most reliable one, providing a trade-off between overfitting and underfitting (Gelman et al., 2020b). For instance, we proposed a linear relationship between cortical excitability and

hemodynamic responses evoked by a finger-tapping task. However, such association might reach a plateau when excitability changes are either too low or too high, suggesting some non-linear models. Moreover, the neurovascular system includes different aspects like excitatory and inhibitory neurons, glial cells, the vasculature components like pericytes (Populations, 2017). The interaction between inhibitory and excitatory neurons, the glial cell mediated signaling pathways, and their role in neurovascular coupling have been simplified in this linear model. A more detailed metabolism model involving blood flow dynamics (Buxton, 2021) may improve our inferences by comparing it with the model proposed in this study. Considering such advanced model comparisons, applied within a Bayesian framework, could be of great interest but was out of the scope of this study. Moreover, we conducted TMS following the recommendations of the International Federation of Clinical Neurophysiology (Rossi et al., 2009), which means our data set should not explore extreme conditions between excitability and hemodynamic response, which are more likely to exhibit eventual nonlinear relationships.

Another limitation of our study was that the M1 excitability was not assessed at the same time as the finger-tapping task, but sequentially, hence we did not propose a fusion model to pool the relationship between cortical excitability and hemodynamic responses at the single-trial level. We considered the mean and variance of MEP amplitudes and HbO/HbR time courses within the whole session as the input for the correlation analysis. This might reduce the resulted correlation values considering additional fluctuations of the baseline excitability and hemodynamic responses. However, since it has been shown that PAS modulated excitability changes could last for more than 30 minutes (Stefan, 2000; Lee et al., 2017), we are confident that our investigation of cortical excitability using MEP after spTMS and hemodynamic responses elicited by finger tapping was indeed still within this PAS effective duration window.

As perspectives for this study, it would be of great interest to investigate the relationship between spTMS evoked HbO/HbR and the corresponding MEP amplitude, when occurring exactly at the same time, therefore, preventing confounds introduced by fluctuations of excitability and hemodynamic responses along the time. Such an investigation may help us in understanding the integrity of neurovascular coupling during the transit cortical excitability change induced by spTMS. Furthermore, the effect of stable cortical excitability changes (induced by PAS) on this integrity can be explored by comparing the spTMS evoked hemodynamic responses before and after PAS interventions. Additionally, since fNIRS data

were recorded during the whole experiments (i.e., also during spTMS and PAS intervention), our data would allow assessing dynamically the evolution of MEP and hemodynamic responses during PAS. However, such analysis would require modeling fNIRS response using advanced deconvolution techniques to handle the overlapping of TMS pulses induced hemodynamic responses (Machado et al., 2021), and will be considered in our future investigations.

5. Conclusion

In this study, we proposed hierarchical Bayesian modeling to investigate the relationship between motor task-related hemodynamic responses and M1 excitability. When compared with a sham control condition, a substantial M1 excitability increase was found after PAS25, and a subtle reduction of M1 excitability was found after PAS10. PAS effects on motor task-related hemodynamic responses were observed mainly around the peak of HbO/HbR time courses. We showed a large probability of positive correlations between PAS effects on MEP amplitudes and hemodynamic responses. Such correlations were also mainly exhibited around the peak of HbO/HbR time courses. Diagnostics of sampling MCMC chains showed no pathological behavior, ensuring the reliability of our results. Finally, this study also demonstrated the power of the Bayesian data analysis when dealing with relatively high variability and small sample size data while providing informative inferences.

Acknowledgments

This work was supported by the Natural Sciences and Engineering Research Council of Canada Discovery Grant Program (CG and JML), an operating grant from the Canadian Institutes for Health Research (CIHR MOP 133619 (CG)), a FRQNT research team grant and a FRQS-Quebec Bio-Imaging Network (QBIN) Pilot Project grant. fNIRS equipment was acquired using grants from NSERC Research Tools and Instrumentation Program and the Canadian Foundation for Innovation (CG). ZC is funded by the Fonds de recherche du Québec – Sante (FRQS) Doctoral Training Scholarship and the PERFORM Graduate Scholarship in Preventive Health Research. GP is funded by Strauss Canada Foundation and a McGill/MNI - Fred Andermann EEG and Epilepsy Fellowship.

Conflict of interest

The authors declare no potential conflict of interest.

References

Aarabi, A., Osharina, V., Wallois, F., 2017. Effect of confounding variables on hemodynamic response function estimation using averaging and deconvolution analysis: An event-related NIRS study. Neuroimage 155, 25–49. https://doi.org/10.1016/j.neuroimage.2017.04.048

Ah Sen, C.B., Fassett, H.J., El-Sayes, J., Turco, C. V, Hameer, M.M., Nelson, A.J., 2017. Active and resting motor threshold are efficiently obtained with adaptive threshold hunting. PLoS One 12. https://doi.org/10.1371/journal.pone.0186007

Ahn, W.-Y., Haines, N., Zhang, L., 2017. Revealing Neurocomputational Mechanisms of Reinforcement Learning and Decision-Making With the hBayesDM Package. Comput. Psychiatry 1, 24. https://doi.org/10.1162/cpsy_a_00002

Allen, E.A., Pasley, B.N., Duong, T., Freeman, R.D., 2007. Transcranial magnetic stimulation elicits coupled neural and hemodynamic consequences. Science (80-.). 317, 1918–1921. https://doi.org/10.1126/science.1146426

Arridge, S.R., 1999. Optical tomography in medical imaging. Inverse Probl. 15, R41. https://doi.org/10.1088/0266-5611/15/2/022

Awiszus, F., Feistner, H., Urbach, D., Bostock, H., 1999. Characterisation of paired-pulse transcranial magnetic stimulation conditions yielding intracortical inhibition or I-wave facilitation using a threshold-hunting paradigm. Exp. Brain Res. 129, 317–324. https://doi.org/10.1007/s002210050901

Bandettini, P.A., Wong, E.C., Hinks, R.S., Tikofsky, R.S., Hyde, J.S., 1992. Time course EPI of human brain function during task activation. Magn. Reson. Med. 25, 390–397. https://doi.org/10.1002/mrm.1910250220

Betancourt, M., 2019. The Convergence of Markov Chain Monte Carlo Methods: From the Metropolis Method to Hamiltonian Monte Carlo. Ann. Phys. 531, 1–6. https://doi.org/10.1002/andp.201700214

Betancourt, M., 2017. A Conceptual Introduction to Hamiltonian Monte Carlo. eprint arXiv:1701.02434 60. https://doi.org/https://arxiv.org/abs/1701.02434

Betancourt, M., 2016. Diagnosing Suboptimal Cotangent Disintegrations in Hamiltonian Monte Carlo. arXiv 1604.00695.

Betancourt, M., Byrne, S., Livingstone, S., Girolami, M., 2017. The geometric foundations of Hamiltonian Monte Carlo. Bernoulli 23, 2257–2298. https://doi.org/10.3150/16-BEJ810

Betancourt, M., Girolami, M., 2015. Hamiltonian Monte Carlo for Hierarchical Models. Curr. Trends Bayesian Methodol. with Appl. 79–101. https://doi.org/10.1201/b18502-5

Bhalerao, S., Kadam, P., 2010. Sample size calculation. Int. J. Ayurveda Res. 1, 55. https://doi.org/10.4103/0974-7788.59946

Boor, C. de, 2001. A Practical Guide to Splines - Revised Edition, Springer-Verlag, New York.

Brooks, S.P., Gelman, A., 1998. General methods for monitoring convergence of iterative simulations. J. Comput. Graph. Stat. 7, 434–455. https://doi.org/10.1080/10618600.1998.10474787

Buxton, R.B., 2021. The thermodynamics of thinking: Connections between neural activity, energy metabolism and blood flow: Thermodynamics of thinking. Philos. Trans. R. Soc. B Biol. Sci. 376. https://doi.org/10.1098/rstb.2019.0624rstb20190624

Cai, Z., Machado, A., Chowdhury, R.A., Spilkin, A., Vincent, T., Aydin, U., Pellegrino, G., Lina, J.-M., Grova, C., 2021a. Diffuse optical reconstructions of NIRS data using Maximum Entropy on the Mean. bioRxiv. https://doi.org/10.1101/2021.02.22.432263

Cai, Z., Pellegrino, G., Spilkin, A., Delaire, E., Uji, M., Abdallah, C., Lina, J., Fecteau, S., Grova, C., 2021b. Hemodynamic Correlates of Fluctuations in Neuronal Excitability□: A Simultaneous Paired Associative Stimulation (PAS) and functional Near Infra-Red Spectroscopy (fNIRS) Study. bioRxiv. https://doi.org/10.1101/2021.09.29.462418

Cai, Z., Uji, M., Aydin, Ü., Pellegrino, G., Spilkin, A., Delaire, É., Abdallah, C., Lina, J., Grova, C., 2021c. Evaluation of a personalized functional near infra-red optical tomography workflow using maximum entropy on the mean. Hum. Brain Mapp. hbm.25566. https://doi.org/10.1002/hbm.25566

Carson, R.G., Kennedy, N.C., 2013. Modulation of human corticospinal excitability by paired associative stimulation. Front. Hum. Neurosci. 7, 1–28. https://doi.org/10.3389/fnhum.2013.00823

Chen, G., Bürkner, P.C., Taylor, P.A., Li, Z., Yin, L., Glen, D.R., Kinnison, J., Cox, R.W., Pessoa, L., 2019a. An integrative Bayesian approach to matrix-based analysis in neuroimaging. Hum. Brain Mapp. 40, 4072–4090. https://doi.org/10.1002/hbm.24686

Chen, G., Padmala, S., Chen, Y., Taylor, P.A., Cox, R.W., Pessoa, L., 2021. To pool or not to pool: Can we ignore cross-trial variability in FMRI? Neuroimage 225, 117496. https://doi.org/10.1016/j.neuroimage.2020.117496

Chen, G., Xiao, Y., Taylor, P.A., Rajendra, J.K., Riggins, T., Geng, F., Redcay, E., Cox, R.W., 2019b. Handling Multiplicity in Neuroimaging Through Bayesian Lenses with Multilevel Modeling. Neuroinformatics 17, 515–545. https://doi.org/10.1007/s12021-018-9409-6

Chiang, T.C., Vaithianathan, T., Leung, T., Lavidor, M., Walsh, V., Delpy, D.T., 2007. Elevated haemoglobin levels in the motor cortex following 1 Hz transcranial magnetic stimulation: A preliminary study. Exp. Brain Res. 181, 555–560. https://doi.org/10.1007/s00221-007-0952-x

Chowdhury, R.A., Lina, J.M., Kobayashi, E., Grova, C., 2013. MEG Source Localization of Spatially Extended Generators of Epileptic Activity: Comparing Entropic and Hierarchical Bayesian Approaches. PLoS One 8, e55969. https://doi.org/10.1371/journal.pone.0055969

Chowdhury, R.A., Merlet, I., Birot, G., Kobayashi, E., Nica, A., Biraben, A., Wendling, F., Lina, J.M., Albera, L., Grova, C., 2016. Complex patterns of spatially extended generators of epileptic activity: Comparison of source localization methods cMEM and 4-ExSo-MUSIC on high resolution EEG and MEG data. Neuroimage 143, 175–195. https://doi.org/10.1016/j.neuroimage.2016.08.044

Corp, D.T., Bereznicki, H.G., Clark, G.M., Youssef, G.J., Fried, P.J., Jannati, A., Davies, C.B., Gomes-Osman, J., Kirkovski, M., Albein-Urios, N., Fitzgerald, P.B., Koch, G., Di Lazzaro, V., Pascual-Leone, A., Enticott, P.G., 2021. Large-scale analysis of interindividual variability in single and paired-pulse TMS data. Clin. Neurophysiol. https://doi.org/10.1016/j.clinph.2021.06.014

Curtin, A., Tong, S., Sun, J., Wang, J., Onaral, B., Ayaz, H., 2019. A systematic review of integrated functional near-infrared spectroscopy (fNIRS) and transcranial magnetic stimulation (TMS) studies. Front. Neurosci. 13. https://doi.org/10.3389/fnins.2019.00084

Dai, N., Kang, H., Jones, G.L., Fiecas, M.B., 2021. A Bayesian latent spatial model for mapping the cortical signature of progression to Alzheimer's disease. Can. J. Stat. 49, 46–62. https://doi.org/10.1002/cjs.11588

Di Pino, G., Pellegrino, G., Assenza, G., Capone, F., Ferreri, F., Formica, D., Ranieri, F., Tombini, M., Ziemann, U., Rothwell, J.C., Di Lazzaro, V., 2014. Modulation of brain plasticity in stroke: A novel model for neurorehabilitation. Nat. Rev. Neurol. 10, 597–608. https://doi.org/10.1038/nrneurol.2014.162

Duane, S., Kennedy, A.D., Pendleton, B.J., Roweth, D., 1987. Hybrid Monte Carlo. Phys. Lett. B 195, 216–222. https://doi.org/10.1016/0370-2693(87)91197-X

Eggebrecht, A.T., White, B.R., Ferradal, S.L., Chen, C., Zhan, Y., Snyder, A.Z., Dehghani, H., Culver, J.P., 2012. A quantitative spatial comparison of high-density diffuse optical tomography and fMRI cortical mapping. Neuroimage 61, 1120–1128. https://doi.org/10.1016/j.neuroimage.2012.01.124

Eilers, P.H.C., Marx, B.D., 2010. Splines, knots, and penalties. Wiley Interdiscip. Rev. Comput. Stat. 2, 637–653. https://doi.org/10.1002/wics.125

Fang, Q., Boas, D.A., 2009. Monte Carlo Simulation of Photon Migration in 3D Turbid Media Accelerated by Graphics Processing Units. Opt. Express 17, 20178. https://doi.org/10.1364/oe.17.020178

Fischl, B., Salat, D.H., Busa, E., Albert, M., Dieterich, M., Haselgrove, C., Van Der Kouwe, A., Killiany, R., Kennedy, D., Klaveness, S., Montillo, A., Makris, N., Rosen, B., Dale, A.M., 2002. Whole brain segmentation: Automated labeling of neuroanatomical structures in the human brain. Neuron 33, 341–355. https://doi.org/10.1016/S0896-6273(02)00569-X

Fonov, V., Evans, A., McKinstry, R., Almli, C., Collins, D., 2009. Unbiased nonlinear average age-appropriate brain templates from birth to adulthood. Neuroimage 47, S102. https://doi.org/10.1016/s1053-8119(09)70884-5

Fonov, V., Evans, A.C., Botteron, K., Almli, C.R., McKinstry, R.C., Collins, D.L., 2011. Unbiased average age-appropriate atlases for pediatric studies. Neuroimage 54, 313–327. https://doi.org/10.1016/j.neuroimage.2010.07.033

Gabry, J., Mahr, T., 2020. bayesplot: Plotting for Bayesian Models.

Gabry, J., Simpson, D., Vehtari, A., Betancourt, M., Gelman, A., 2019. Visualization in Bayesian workflow. J. R. Stat. Soc. Ser. A Stat. Soc. 182, 389–402. https://doi.org/10.1111/rssa.12378

Gelfand, A.E., Smith, A.F.M., 1990. Sampling-based approaches to calculating marginal

densities. J. Am. Stat. Assoc. 85, 398–409. https://doi.org/10.1080/01621459.1990.10476213

Gelman, A., Carlin, J., 2014. Beyond Power Calculations: Assessing Type S (Sign) and Type M (Magnitude) Errors. Perspect. Psychol. Sci. 9, 641–651. https://doi.org/10.1177/1745691614551642

Gelman, A., Carlin, J.B., Stern, H.S., Dunson, D.B., Vehtari, A., Rubin, D.B., 2013. Bayesian Data Analysis Third edition, 3rd ed. CRC press.

Gelman, A., Hill, J., Vehtari, A., 2020a. Regression and other stories. Cambridge University Press.

Gelman, A., Jakulin, A., Pittau, M.G., Su, Y.S., 2008. A weakly informative default prior distribution for logistic and other regression models. Ann. Appl. Stat. 2, 1360–1383. https://doi.org/10.1214/08-AOAS191

Gelman, A., Rubin, D.B., 1992. Inference from iterative simulation using multiple sequences. Stat. Sci. 7, 457–472. https://doi.org/10.1214/ss/1177011136

Gelman, A., Simpson, D., Betancourt, M., 2017. The prior can often only be understood in the context of the likelihood. Entropy 19, 1–13. https://doi.org/10.3390/e19100555

Gelman, A., Vehtari, A., Simpson, D., Margossian, C.C., Carpenter, B., Yao, Y., Kennedy, L., Gabry, J., Bürkner, P.C., Modrák, M., 2020b. Bayesian workflow. arXiv.

Geman, S., Geman, D., 1984. Stochastic Relaxation, Gibbs Distributions, and the Bayesian Restoration of Images. IEEE Trans. Pattern Anal. Mach. Intell. PAMI-6, 721–741. https://doi.org/10.1109/TPAMI.1984.4767596

Glover, G.H., 2011. Overview of functional magnetic resonance imaging. Neurosurg. Clin. N. Am. https://doi.org/10.1016/j.nec.2010.11.001

Grova, C., Aiguabella, M., Zelmann, R., Lina, J.M., Hall, J.A., Kobayashi, E., 2016. Intracranial EEG potentials estimated from MEG sources: A new approach to correlate MEG and iEEG data in epilepsy. Hum. Brain Mapp. 37, 1661–1683. https://doi.org/10.1002/hbm.23127

Grova, C., Makni, S., Flandin, G., Ciuciu, P., Gotman, J., Poline, J.B., 2006. Anatomically informed interpolation of fMRI data on the cortical surface. Neuroimage 31, 1475–1486. https://doi.org/10.1016/j.neuroimage.2006.02.049

Hashemi, M., Vattikonda, A.N., Sip, V., Guye, M., Bartolomei, F., Woodman, M.M., Jirsa, V.K., 2020. The Bayesian Virtual Epileptic Patient: A probabilistic framework designed to infer the spatial map of epileptogenicity in a personalized large-scale brain model of epilepsy spread. Neuroimage 217, 116839. https://doi.org/10.1016/j.neuroimage.2020.116839

Hastie, T.J., 2017. Generalized additive models, in: Statistical Models in S. https://doi.org/10.1201/9780203738535

Hattemer, K., Knake, S., Reis, J., Rochon, J., Oertel, W.H., Rosenow, F., Hamer, H.M., 2007. Excitability of the motor cortex during ovulatory and anovulatory cycles: A transcranial magnetic stimulation study. Clin. Endocrinol. (Oxf). 66, 387–393. https://doi.org/10.1111/j.1365-2265.2007.02744.x

Hedrich, T., Pellegrino, G., Kobayashi, E., Lina, J.M., Grova, C., 2017. Comparison of the spatial resolution of source imaging techniques in high-density EEG and MEG. Neuroimage 157, 531–544. https://doi.org/10.1016/j.neuroimage.2017.06.022

Heers, M., Chowdhury, R.A., Hedrich, T., Dubeau, F., Hall, J.A., Lina, J.M., Grova, C., Kobayashi, E., 2016. Localization Accuracy of Distributed Inverse Solutions for Electric and Magnetic Source Imaging of Interictal Epileptic Discharges in Patients with Focal Epilepsy. Brain Topogr. 29, 162–181. https://doi.org/10.1007/s10548-014-0423-1

Jasdzewski, G., Strangman, G., Wagner, J., Kwong, K.K., Poldrack, R.A., Boas, D.A., 2003. Differences in the hemodynamic response to event-related motor and visual paradigms as measured by near-infrared spectroscopy. Neuroimage 20, 479–488. https://doi.org/10.1016/S1053-8119(03)00311-2

Jöbsis, F.F., 1977. Noninvasive, infrared monitoring of cerebral and myocardial oxygen sufficiency and circulatory parameters. Science (80-.). 198, 1264–1266. https://doi.org/10.1126/science.929199

Kay, M., 2020. tidybayes: Tidy Data and Geoms for Bayesian Models. R package version 2.3.0. https//mjskay.github.io/tidybayes/. DOI 10.5281/zenodo.1308151. https://doi.org/10.5281/zenodo.1308151

Kriváneková, L., Baudrexel, S., Bliem, B., Ziemann, U., 2013. Relation of brain stimulation induced changes in MEP amplitude and BOLD signal. Brain Stimul. 6, 330–339. https://doi.org/10.1016/j.brs.2012.06.004

Kwong, K.K., Belliveau, J.W., Chesler, D.A., Goldberg, I.E., Weisskoff, R.M., Poncelet, B.P., Kennedy, D.N., Hoppel, B.E., Cohen, M.S., Turner, R., Cheng -, H.M., Brady, T.J., Rosen, B.R., 1992. Dynamic magnetic resonance imaging of human brain activity during primary sensory stimulation. Proc. Natl. Acad. Sci. U. S. A. 89, 5675–5679. https://doi.org/10.1073/pnas.89.12.5675

Lee, J.C., Croarkin, P.E., Ameis, S.H., Sun, Y., Blumberger, D.M., Rajji, T.K., Daskalakis, Z.J., 2017. Paired-Associative Stimulation-Induced Long-term Potentiation-Like Motor Cortex Plasticity in Healthy Adolescents. Front. Psychiatry 8, 1–8. https://doi.org/10.3389/fpsyt.2017.00095

Levy, W.B., Steward, O., 1983. Temporal contiguity requirements for long-term associative potentiation/depression in the hippocampus. Neuroscience 8, 791–797. https://doi.org/10.1016/0306-4522(83)90010-6

Lewandowski, D., Kurowicka, D., Joe, H., 2009. Generating random correlation matrices based on vines and extended onion method. J. Multivar. Anal. 100, 1989–2001. https://doi.org/10.1016/j.jmva.2009.04.008

López-Alonso, V., Cheeran, B., Río-Rodríguez, D., Fernández-Del-Olmo, M., 2014. Inter-individual variability in response to non-invasive brain stimulation paradigms. Brain Stimul. 7, 372–380. https://doi.org/10.1016/j.brs.2014.02.004

Machado, A., Cai, Z., Pellegrino, G., Marcotte, O., Vincent, T., Lina, J.-M., Kobayashi, E., Grova, C., 2018. Optimal positioning of optodes on the scalp for personalized functional near-infrared spectroscopy investigations. J. Neurosci. Methods 309, 91–108. https://doi.org/10.1016/J.JNEUMETH.2018.08.006

Machado, A., Cai, Z., Vincent, T., Pellegrino, G., Lina, J.M., Kobayashi, E., Grova, C., 2021. Deconvolution of hemodynamic responses along the cortical surface using personalized functional near infrared spectroscopy. Sci. Rep. 1–19. https://doi.org/10.1038/s41598-021-85386-0

Machado, A., Marcotte, O., Lina, J.M., Kobayashi, E., Grova, C., 2014. Optimal optode montage on electroencephalography/functional near-infrared spectroscopy caps dedicated to study epileptic discharges. J. Biomed. Opt. 19, 026010. https://doi.org/10.1117/1.JBO.19.2.026010

Mariorenzi, R., Zarola, F., Caramia, M.D., Paradiso, C., Rossini, P.M., 1991. Non-invasive

evaluation of central motor tract excitability changes following peripheral nerve stimulation in healthy humans. Electroencephalogr. Clin. Neurophysiol. Evoked Potentials 81, 90–101. https://doi.org/10.1016/0168-5597(91)90002-F

McElreath, R., 2020. Statistical Rethinking, 2nd ed, CRC Press. https://doi.org/10.1201/9781315372495

Näsi, T., Mäki, H., Kotilahti, K., Nissilä, I., Haapalahti, P., Ilmoniemi, R.J., 2011. Magnetic-stimulation-related physiological artifacts in hemodynamic near-infrared spectroscopy signals. PLoS One 6. https://doi.org/10.1371/journal.pone.0024002

Navarro De Lara, L.I., Windischberger, C., Kuehne, A., Woletz, M., Sieg, J., Bestmann, S., Weiskopf, N., Strasser, B., Moser, E., Laistler, E., 2015. A novel coil array for combined TMS/fMRI experiments at 3 T. Magn. Reson. Med. 74, 1492–1501. https://doi.org/10.1002/mrm.25535

Neal, R.M., 2010. MCMC Using Hamiltonian Dynamics. Handb. Markov Chain Monte Carlo 54, 113–162.

Neal, R.M., 2003. Slice sampling. Ann. Stat. 31, 705–767. https://doi.org/10.2307/3448415

Neal, R.M., 1998. Regression and Classification Using Gaussian Process Priors. Bayesian Stat. 6, 475–501.

Novi, S.L., Forero, E.J., Rubianes Silva, J.A.I., de Souza, N.G.S.R., Martins, G.G., Quiroga, A., Wu, S.T., Mesquita, R.C., 2020. Integration of Spatial Information Increases Reproducibility in Functional Near-Infrared Spectroscopy. Front. Neurosci. 14, 1–12. https://doi.org/10.3389/fnins.2020.00746

Papaspiliopoulos, O., Roberts, G.O., Sköld, M., 2007. A general framework for the parametrization of hierarchical models. Stat. Sci. https://doi.org/10.1214/088342307000000014

Pellegrino, G., Hedrich, T., Porras-Bettancourt, M., Lina, J.M., Aydin, Ü., Hall, J., Grova, C., Kobayashi, E., 2020. Accuracy and spatial properties of distributed magnetic source imaging techniques in the investigation of focal epilepsy patients. Hum. Brain Mapp. 41, 3019–3033. https://doi.org/10.1002/hbm.24994

Pellegrino, G., Machado, A., von Ellenrieder, N., Watanabe, S., Hall, J.A., Lina, J.M., Kobayashi, E., Grova, C., 2016. Hemodynamic response to interictal epileptiform discharges addressed by personalized EEG-fNIRS recordings. Front. Neurosci. 10, 102.

https://doi.org/10.3389/fnins.2016.00102

Penny, W.D., Friston, K.J., Ashburner, J.T., Kiebel, S.J., Nichols, T.E., 2011. Statistical parametric mapping: the analysis of functional brain images, Elsevier.

Piper, S.K., Krueger, A., Koch, S.P., Mehnert, J., Habermehl, C., Steinbrink, J., Obrig, H., Schmitz, C.H., 2014. A wearable multi-channel fNIRS system for brain imaging in freely moving subjects. Neuroimage 85, 64–71. https://doi.org/10.1016/j.neuroimage.2013.06.062

Populations, T. variation and factors influencing vertical migration behavior in D., 2017. The neurovascular unit coming of age: a journey through neurovascular coupling in health and disease Costantino 96(1): 17–42. doi:10.1016/j.neuron.2017.07.030. The neurovascular unit coming of age: a journe. Physiol. Behav. 176, 139–148. https://doi.org/10.1016/j.neuron.2017.07.030.The

R Core Team, 2020. R: A Language and Environment for Statistical Computing.

Raffin, E., Pellegrino, G., Di Lazzaro, V., Thielscher, A., Siebner, H.R., 2015. Bringing transcranial mapping into shape: Sulcus-aligned mapping captures motor somatotopy in human primary motor hand area. Neuroimage 120, 164–175. https://doi.org/10.1016/j.neuroimage.2015.07.024

Ridding, M.C., Rothwell, J.C., 2007. Is there a future for therapeutic use of transcranial magnetic stimulation? Nat. Rev. Neurosci. https://doi.org/10.1038/nrn2169

Roberts, G.O., Rosenthal, J.S., 2004. General state space Markov chains and MCMC algorithms. Probab. Surv. 1, 20–71. https://doi.org/10.1214/154957804100000024

Rossi, S., Hallett, M., Rossini, P.M., Pascual-Leone, A., Avanzini, G., Bestmann, S., Berardelli, A., Brewer, C., Canli, T., Cantello, R., Chen, R., Classen, J., Demitrack, M., Di Lazzaro, V., Epstein, C.M., George, M.S., Fregni, F., Ilmoniemi, R., Jalinous, R., Karp, B., Lefaucheur, J.P., Lisanby, S., Meunier, S., Miniussi, C., Miranda, P., Padberg, F., Paulus, W., Peterchev, A., Porteri, C., Provost, M., Quartarone, A., Rotenberg, A., Rothwell, J., Ruohonen, J., Siebner, H., Thut, G., Valls-Solè, J., Walsh, V., Ugawa, Y., Zangen, A., Ziemann, U., 2009. Safety, ethical considerations, and application guidelines for the use of transcranial magnetic stimulation in clinical practice and research. Clin. Neurophysiol. https://doi.org/10.1016/j.clinph.2009.08.016

Rossini, P.M., Burke, D., Chen, R., Cohen, L.G., Daskalakis, Z., Di Iorio, R., Di Lazzaro, V.,

Ferreri, F., Fitzgerald, P.B., George, M.S., Hallett, M., Lefaucheur, J.P., Langguth, B., Matsumoto, H., Miniussi, C., Nitsche, M.A., Pascual-Leone, A., Paulus, W., Rossi, S., Rothwell, J.C., Siebner, H.R., Ugawa, Y., Walsh, V., Ziemann, U., 2015. Non-invasive electrical and magnetic stimulation of the brain, spinal cord, roots and peripheral nerves: Basic principles and procedures for routine clinical and research application: An updated report from an I.F.C.N. Committee. Clin. Neurophysiol. 126, 1071–1107. https://doi.org/10.1016/j.clinph.2015.02.001

Rubin, D.B., 2004. Multiple imputation for nonresponse in surveys. John Wiley & Sons.

Schmitz, C.H., Klemer, D.P., Hardin, R., Katz, M.S., Pei, Y., Graber, H.L., Levin, M.B., Levina, R.D., Franco, N.A., Solomon, W.B., Barbour, R.L., 2005. Design and implementation of dynamic near-infrared optical tomographic imaging instrumentation for simultaneous dual-breast measurements. Appl. Opt. 44, 2140. https://doi.org/10.1364/AO.44.002140

Schneider, P., Piper, S., Schmitz, C.H., Schreiter, N.F., Volkwein, N., Lüdemann, L., Malzahn, U., Poellinger, A., 2011. Fast 3D near-infrared breast imaging using indocyanine green for detection and characterization of breast lesions. RoFo Fortschritte auf dem Gebiet der Rontgenstrahlen und der Bildgeb. Verfahren 183, 956–963. https://doi.org/10.1055/s-0031-1281726

Scholkmann, F., Kleiser, S., Metz, A.J., Zimmermann, R., Mata Pavia, J., Wolf, U., Wolf, M., 2014. A review on continuous wave functional near-infrared spectroscopy and imaging instrumentation and methodology. Neuroimage. https://doi.org/10.1016/j.neuroimage.2013.05.004

Seewoo, B.J., Feindel, K.W., Etherington, S.J., Rodger, J., 2019. Frequency-specific effects of low-intensity rTMS can persist for up to 2 weeks post-stimulation: A longitudinal rs-fMRI/MRS study in rats. Brain Stimul. 12, 1526–1536. https://doi.org/10.1016/j.brs.2019.06.028

Siebner, H.R., Bergmann, T.O., Bestmann, S., Massimini, M., Johansen-Berg, H., Mochizuki, H., Bohning, D.E., Boorman, E.D., Groppa, S., Miniussi, C., Pascual-Leone, A., Huber, R., Taylor, P.C.J., Ilmoniemi, R.J., De Gennaro, L., Strafella, A.P., Kähkönen, S., Klöppel, S., Frisoni, G.B., George, M.S., Hallett, M., Brandt, S.A., Rushworth, M.F., Ziemann, U., Rothwell, J.C., Ward, N., Cohen, L.G., Baudewig, J., Paus, T., Ugawa, Y., Rossini, P.M., 2009. Consensus paper: Combining transcranial stimulation with

neuroimaging. Brain Stimul. 2, 58–80. https://doi.org/10.1016/j.brs.2008.11.002

Sotero, R.C., Trujillo-Barreto, N.J., 2007. Modelling the role of excitatory and inhibitory neuronal activity in the generation of the BOLD signal. Neuroimage 35, 149–165. https://doi.org/10.1016/j.neuroimage.2006.10.027

Stan Development Team, 2020a. Stan Modeling Language Users Guide and Reference Manual, 2.25.0.

Stan Development Team, 2020b. RStan: the R interface to Stan, 2.21.2.

Stefan, K., 2000. Induction of plasticity in the human motor cortex by paired associative stimulation. Brain 123, 572–584. https://doi.org/10.1093/brain/123.3.572

Steinbrink, J., Villringer, A., Kempf, F., Haux, D., Boden, S., Obrig, H., 2006. Illuminating the BOLD signal: combined fMRI-fNIRS studies. Magn. Reson. Imaging 24, 495–505. https://doi.org/10.1016/j.mri.2005.12.034

Suppa, A., Quartarone, A., Siebner, H., Chen, R., Di Lazzaro, V., Del Giudice, P., Paulus, W., Rothwell, J.C., Ziemann, U., Classen, J., 2017. The associative brain at work: Evidence from paired associative stimulation studies in humans. Clin. Neurophysiol. 128, 2140–2164. https://doi.org/10.1016/j.clinph.2017.08.003

Tadel, F., Baillet, S., Mosher, J.C., Pantazis, D., Leahy, R.M., 2011. Brainstorm: A user-friendly application for MEG/EEG analysis. Comput. Intell. Neurosci. 2011, 879716. https://doi.org/10.1155/2011/879716

Thomson, R.H., Cleve, T.J., Bailey, N.W., Rogasch, N.C., Maller, J.J., Daskalakis, Z.J., Fitzgerald, P.B., 2013. Blood oxygenation changes modulated by coil orientation during prefrontal transcranial magnetic stimulation. Brain Stimul. 6, 576–581. https://doi.org/10.1016/j.brs.2012.12.001

Tik, M., Hoffmann, A., Sladky, R., Tomova, L., Hummer, A., Navarro de Lara, L., Bukowski, H., Pripfl, J., Biswal, B., Lamm, C., Windischberger, C., 2017. Towards understanding rTMS mechanism of action: Stimulation of the DLPFC causes network-specific increase in functional connectivity. Neuroimage 162, 289–296. https://doi.org/10.1016/j.neuroimage.2017.09.022

Tsang, P., Bailey, A.Z., Nelson, A.J., 2015. Rapid-rate paired associative stimulation over the primary somatosensory cortex. PLoS One 10, e0120731. https://doi.org/10.1371/journal.pone.0120731

Vehtari, A., Gelman, A., Simpson, D., Carpenter, B., Bürkner, P.C., 2020. Rank-normalization, folding, and localization: An improved R for assessing convergence of MCMC. Bayesian Anal. https://doi.org/10.1214/20-ba1221

Ventrucci, M., Rue, H., 2016. Penalized complexity priors for degrees of freedom in Bayesian P-splines. Stat. Modelling 16, 429–453. https://doi.org/10.1177/1471082X16659154

Wang, W.T., Xu, B., Butman, J.A., 2017. Improved SNR for combined TMS-fMRI: A support device for commercially available body array coil. J. Neurosci. Methods 289, 1–7. https://doi.org/10.1016/j.jneumeth.2017.06.020

Wickham, H., Averick, M., Bryan, J., Chang, W., McGowan, L.D., François, R., Grolemund, G., Hayes, A., Henry, L., Hester, J., Kuhn, M., Pedersen, T.L., Miller, E., Bache, S.M., Müller, K., Ooms, J., Robinson, D., Seidel, D.P., Spinu, V., Takahashi, K., Vaughan, D., Wilke, C., Woo, K., Yutani, H., 2019. Welcome to the tidyverse. J. Open Source Softw. 4, 1686. https://doi.org/10.21105/joss.01686

Witt, S.T., Laird, A.R., Meyerand, M.E., 2008. Functional neuroimaging correlates of finger-tapping task variations: An ALE meta-analysis. Neuroimage 42, 343–356. https://doi.org/10.1016/j.neuroimage.2008.04.025

Wolters, A., Schmidt, A., Schramm, A., Zeller, D., Naumann, M., Kunesch, E., Benecke, R., Reiners, K., Classen, J., 2005. Timing-dependent plasticity in human primary somatosensory cortex. J. Physiol. 565, 1039–1052. https://doi.org/10.1113/jphysiol.2005.084954

Yamanaka, K., Yamagata, B., Tomioka, H., Kawasaki, S., Mimura, M., 2010. Transcranial magnetic stimulation of the parietal cortex facilitates spatial working memory: Near-infrared spectroscopy study. Cereb. Cortex 20, 1037–1045. https://doi.org/10.1093/cercor/bhp163

Yu, L., Nina-Paravecino, F., Kaeli, D., Fang, Q., 2018. Scalable and massively parallel Monte Carlo photon transport simulations for heterogeneous computing platforms. J. Biomed. Opt. 23, 1. https://doi.org/10.1117/1.jbo.23.1.010504

Yücel, M.A., Selb, J., Boas, D.A., Cash, S.S., Cooper, R.J., 2014. Reducing motion artifacts for long-term clinical NIRS monitoring using collodion-fixed prism-based optical fibers. Neuroimage 85, 192–201. https://doi.org/10.1016/j.neuroimage.2013.06.054

Yücel, M.A., von Lühmann, A., Scholkmann, F., Gervain, J., Dan, I., Ayaz, H., Boas, D., Cooper, R.J., Culver, J., Elwell, C.E., Eggebrecht, A., Franceschini, M.A., Grova, C., Homae, F., Lesage, F., Obrig, H., Tachtsidis, I., Tak, S., Tong, Y., Torricelli, A., Wabnitz, H., Wolf, M., 2020. Best Practices for fNIRS publications. Neurophotonics (in revisi.

Zeff, B.W., White, B.R., Dehghani, H., Schlaggar, B.L., Culver, J.P., 2007. Retinotopic mapping of adult human visual cortex with high-density diffuse optical tomography. Proc. Natl. Acad. Sci. 104, 12169–12174. https://doi.org/10.1073/pnas.0611266104

Appendices

Appendix 1 fNIRS data processing

Raw fNIRS data were first preprocessed following standard recommendations (Yücel et al., 2020): a) bad channel rejections of channels exhibiting either a negative raw amplitude during the whole time course and a coefficient of variation (CV) larger than 8% (Schmitz et al., 2005; Schneider et al., 2011; Eggebrecht et al., 2012; Piper et al., 2014): b) linear regression of superficial physiological fluctuations using the average of all proximity channels (Zeff et al., 2007); c) band-pass filtering (i.e., 0.01Hz to 0.1Hz) using a 3rd order Butterworth filter (zero-phase); d) conversion in optical density changes (i.e., ΔOD) using logarithm conversion; e) ΔOD epochs extraction within a time window ranging from -10s to 30s around task onsets. Instead of the conventional process averaging extracted ΔOD epochs, we then conducted a resampling process to estimate not one but a set of 'possible' averaged ΔODs (Cai et al., 2021b). Our rationale was to propose an evaluation preserving the intrinsic variance of averaged ΔOD related to the underlying physiological fluctuations and eventual measurement errors such as motion artifacts. To do so, we first averaged 16 out of 20 preprocessed ΔOD epochs for all possible unique combinations (i.e., $C_{20}^{16} = 4845$ possibilities). Then, the averaged signal to noise ratio (SNR) of the resulting averaged ΔODs, for each wavelength, was estimated as the peak amplitude over the averaged standard deviation of baseline (within -10s to 0s) among all channels. Lastly, we selected 101 of these resampled averaged ΔODs, distributed around the median SNR (50 averaged below and 50 averaged above the median SNR), to obtain a distribution of 'possible' responses evoked by one finger-tapping run. The selection of 16 blocks out of 20 trials and 101 resampled averaged ΔODs maintained a good coverage of the data distribution. This number was empirically defined according to the observation that usually there were less than four blocks contaminated with artifacts in one finger-tapping run. Selecting sub-averaged trials around the median SNR ensured a good representation of fNIRS responses while discarding artifacts in the meantime. Indeed, in artifacts contaminated data, large motion artifacts would result in high SNR of corresponding sub-averaged trials.

We then applied 3D fNIRS reconstruction workflow using personalized optimal montage and maximum entropy on the mean (MEM), as further described and validated in our earlier work (Cai et al., 2021c), to the 101 sub-averaged ΔODs. Therefore, 'all possible' HbO/HbR responses for each finger-tapping run were reconstructed as spatiotemporal maps along the

cortical surface. To do so, the subject-specific fNIRS forward model was first estimated according to the following steps: a) 5 tissues head segmentation (e.g., scalp, skull, Cerebrospinal fluid, grey matter and white matter) calculated using FreeSurfer6.0 (Fischl et al., 2002) (https://surfer.nmr.mgh.harvard.edu) and SPM12 (Penny et al., 2011) (https://www.fil.ion.ucl.ac.uk/spm/software/spm12/); b) light fluences at each optode location, and for each wavelength (i.e., 685nm and 830nm), were calculated by simulating 10^8 photons, using MCXLAB toolbox - a Monte Carlo photon simulator for modeling light transport in 3D turbid media, developed by Fang and Boas, 2009 and Yu et al., 2018; c) sensitivity of each voxel was computed using the adjoint formulation and was normalized by Rytov approximation (Arridge, 1999); d) surface space sensitivity was finally obtained by projecting volumetric sensitivity map to subject's cortical surface (i.e., mid-surface, a middle layer of the gray matter, between pia mater and gray-white matter interface, 25,000 vertices) using the Voronoi based method proposed by Grova et al., 2006. Finally, each of 101 averaged ΔOD epoch was down-sampled to 2Hz and MEM method proposed previously by our group for fNIRS reconstruction (Cai et al., 2021a, 2021c) was applied to estimate the HbO/HbR spatiotemporal maps (0s to 30s) along the subject-specific cortical surface.

Supplementary material

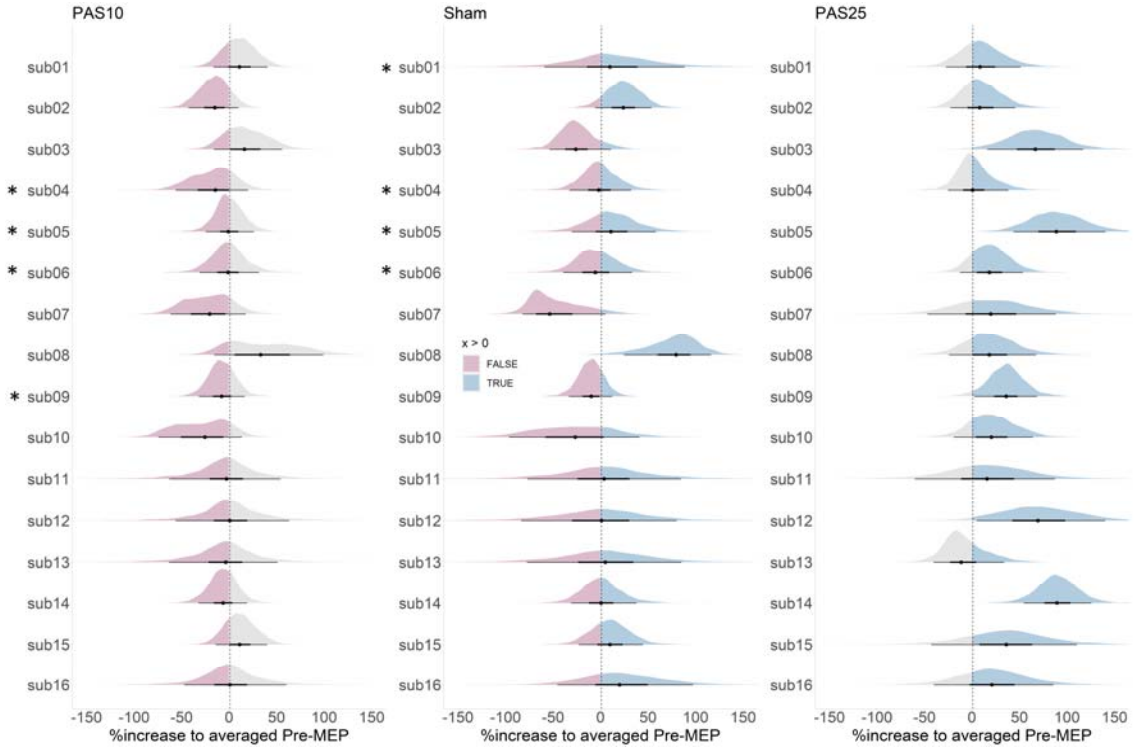

Fig.S1. PAS effects on M1 excitability at the individual level*. Each column presents the individual level posterior distribution of the intervention effect from PAS10, sham and PAS25, respectively. Posterior predictive simulations of post-PAS MEP amplitudes were conducted by assuming the same pre-PAS MEP amplitude for all subjects, i.e., the averaged pre-PAS MEP amplitude obtained for all subjects over all 40 sessions. The blue area represents the probability of obtaining a relative increase (in%) for the post-PAS MEP amplitude when compared to the pre-PAS MEP amplitude, whereas the pink area represents the probability of obtaining a relative decrease (in %). The black dot represents the median of each posterior distribution, and the surrounding bars show the corresponding 50% and 90% credibility intervals. Overall, large between-subject variability can be observed for both interventions. Note that missing sessions were also included using posterior predictive simulations within the model, based on prior distributions and partial pooled information from other sessions. * indicate the missing runs that were imputed by the model.*